

# Systematic review of reconstruction techniques for accelerated quantitative MRI

Banafshe Shafieizargar<sup>1,2</sup>  | Riway Byanju<sup>3</sup>  | Jan Sijbers<sup>1,2</sup>  | Stefan Klein<sup>3</sup>  | Arnold J. den Dekker<sup>1,2</sup>  | Dirk H. J. Poot<sup>3</sup> 

<sup>1</sup>imec-Vision Lab, Department of Physics, University of Antwerp, Antwerp, Belgium

<sup>2</sup> $\mu$ NEURO Research Centre of Excellence, University of Antwerp, Antwerp, Belgium

<sup>3</sup>Department of Radiology and Nuclear Medicine, Erasmus MC, Rotterdam, The Netherlands

## Correspondence

Banafshe Shafieizargar, imec-Vision Lab, Department of Physics, University of Antwerp, Universiteitsplein 1, Antwerp, Belgium.

Email: [banafshe.shz@gmail.com](mailto:banafshe.shz@gmail.com)

## Funding information

Fonds Wetenschappelijk Onderzoek, Grant/Award Number: G084217N; H2020 Marie Skłodowska-Curie Actions, Grant/Award Number: 76451; SEP BOF, Grant/Award Number: FFB210120

**Purpose:** To systematically review the techniques that address undersampling artifacts in accelerated quantitative magnetic resonance imaging (qMRI).

**Methods:** A literature search was conducted using the Embase, Medline, Web of Science Core Collection, Coherence Central Register of Controlled Trials, and Google Scholar databases for studies, published before July 2022 proposing reconstruction techniques for accelerated qMRI. Studies are reviewed according to inclusion criteria, and included studies are categorized based on the methodology used.

**Results:** A total of 292 studies included in the review are categorized. A technical overview of each category is provided, and the categories are described in a unified mathematical framework. The distribution of the reviewed studies over time, application domain, and parameters of interest is illustrated.

**Conclusion:** An increasing trend in the number of articles that propose new techniques for accelerated qMRI reconstruction indicates the importance of acceleration in qMRI. The techniques are mostly validated for relaxometry parameters and brain scans. The categories of techniques are compared based on theoretical grounds, highlighting existing trends and potential gaps in the field.

## KEYWORDS

image reconstruction, MRI, parameter estimation, quantitative MRI

## 1 | INTRODUCTION

Quantitative MRI (qMRI) measures tissue properties such as diffusion, relaxation times, myelin water fraction, and perfusion.<sup>1</sup> qMRI produces maps of calibrated physical parameters expressed in physical units that are reproducible across the scanner.<sup>2</sup> Conventionally, qMRI reconstruction consists of a two-step procedure. The

first step reconstructs multiple images from the acquired k-space data. For each image to be reconstructed, the corresponding k-space data is acquired with unique acquisition settings such as echo time, repetition time, or diffusion weightings. These different acquisition settings lead to differently weighted reconstructed images, that is, images with different contrasts. In what follows, these images will be referred to as contrast images. The

Banafshe Shafieizargar and Riway Byanju contributed equally to this work.

Arnold J. den Dekker and Dirk H. J. Poot contributed equally to this study.

This is an open access article under the terms of the [Creative Commons Attribution](https://creativecommons.org/licenses/by/4.0/) License, which permits use, distribution and reproduction in any medium, provided the original work is properly cited.

© 2023 The Authors. *Magnetic Resonance in Medicine* published by Wiley Periodicals LLC on behalf of International Society for Magnetic Resonance in Medicine.

second step estimates the qMRI parameters by fitting a signal model to the reconstructed contrast images.

Acquisition of multiple contrast images traditionally requires a long scan time, which limits the clinical application of qMRI. Reducing this time has been an important research focus over recent years. Sampling only part of the k-space for each of the contrast images to be reconstructed, that is, undersampling, is one way to shorten the scan time. However, substantial undersampling of the k-space leads to ill-posed reconstruction problems for the individual contrast images, causing artifacts in the reconstructed images.

Acquiring data from the same object with different contrasts produces shared information across the contrasts that can be exploited to improve the qMRI reconstruction of the undersampled data. The different qMRI reconstruction techniques differ from each other in the way they exploit shared information across the contrasts. The multitude of reconstruction techniques and their respective advantages and limitations give rise to the question of to what extent they are different and whether some of these techniques can be advantageously combined. Moreover, as techniques are typically presented for specific applications, the suitability to different applications can be hard to appreciate. Furthermore, the reconstruction techniques are usually introduced using different terminologies, which complicates their comparison. Review studies on qMRI reconstruction techniques are typically specific to a class of techniques such as compressed sensing,<sup>3</sup> MR fingerprinting<sup>4-6</sup> or deep-learning.<sup>7,8</sup> Alternatively, they are specific to a particular class of parameters of interest, such as relaxometry,<sup>7,9-12</sup> or diffusion<sup>13</sup> parameters, or to a particular application domain, such as the knee,<sup>14</sup> or cardiac and abdominal imaging.<sup>15</sup> To facilitate the comparison among different reconstruction techniques used for accelerated qMRI, the current work presents a systematic review that provides a technical overview of the existing techniques, without confining to any specific parameter or application domain, and categorizes them based on methodology. Moreover, all categories are described in a unified mathematical framework.

This systematic review was conducted following the PRISMA 2020 guidelines.<sup>16</sup> The methodology used for the systematic review is introduced in Section 2. Next, Section 3 describes the mathematical formulation of conventional two-step qMRI. Section 4 provides the mathematical formulation of the categorized reviewed techniques and describes how each technique is adjusted to address specific reconstruction issues. In Section 5, a graphical representation of the categorized techniques is provided. Finally, Section 6 provides a discussion of the trends observed in the reviewed techniques, limitations of this work, and directions for future research.

## 2 | METHODS

The systematic review was performed in four phases, which are discussed in the four subsections below and depicted in Figure 1.

### 2.1 | Identification

A literature search was conducted in the following databases: Embase, Medline, Web of Science Core Collection, Coherence Central Register of Controlled Trials, and Google Scholar. The search query was compiled with the help of a librarian specialized in performing systematic reviews. The study was registered in [Prospero](#) with id CRD42021242450. The search query used was based on a combination of four main segments, combined with an *AND* statement. The first segment included words related to “MRI,” “MR fingerprinting,” and “quantitative MRI.” The second segment included words associated with different “reconstruction” techniques to select the papers that deal with image reconstruction. The third segment referred to the qMRI tissue parameters such as  $T_1$ ,  $T_2$ , and diffusion parameters. The last segment was designed to select the works that deal with image reconstruction and parameter estimation. The exact search query for each database is provided in Table A2 in the Appendix. For the search conducted in Google Scholar, the first 200 results were initially selected. Among those 200 results, the ones that were not found previously were added to the results of the other databases. The final search was performed on July 7, 2022 and was confined to articles published in English, without restriction on the publication date. This led to the identification of 4190 papers.

### 2.2 | Screening

The search results were examined based on their title and abstracts by two authors (Banafshe Shafieizargar and Riway Bhanju) independently. Papers were selected when meeting all of the following inclusion criteria:

1. Focusing on qMRI parameter estimation.
2. Accelerating data acquisition by undersampling the k-space.
3. Exploiting the joint information between contrasts to avoid undersampling artifacts.
4. Novel reconstruction and/or parameter estimation technique or improvement of an existing technique other than improvement based on better hardware, in comparison to conventional qMRI reconstruction.

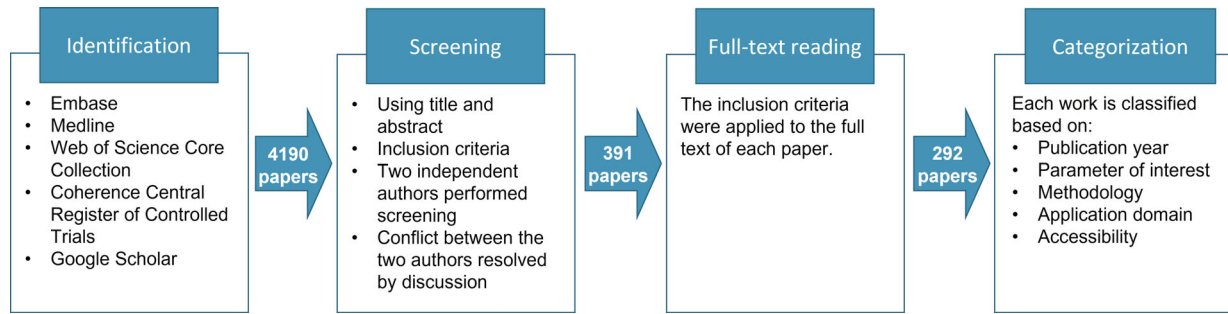


FIGURE 1 Flow chart showing the selection of articles.

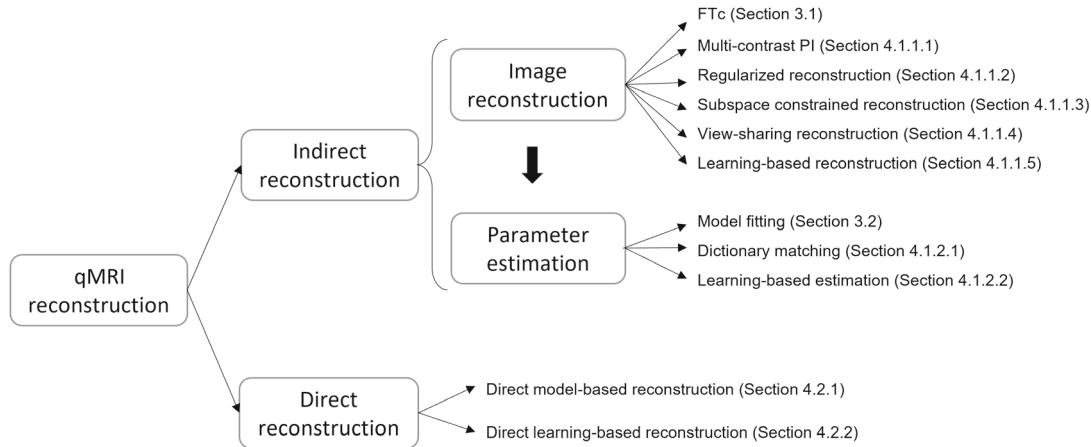


FIGURE 2 Categorization of the techniques reviewed in the current study.

## 5. Including a detailed description of the proposed image reconstruction and/or parameter estimation technique.

If it was unclear whether a paper met a particular criterion from the information in the abstract, then the criterion was considered fulfilled. This phase led to the selection of 391 papers.

## 2.3 | Full-text reading

The full-text of each paper selected during the screening phase was read by one of the two authors who also performed the screening (Banafshe Shafieizargar and Riwanj Byanju). If during or after full-text reading it was concluded that not all criteria of Section 2.2 were met, the paper was excluded. This led to the exclusion of 99 papers so finally, 292 papers were selected for the current study.

## 2.4 | Categorization

In this final phase, the selected works were categorized based on the year of publication, parameter of interest, methodology, application domain, and accessibility

(i.e., a public link to the implemented code and/or acquired dataset).

The methodologies proposed in the selected papers were categorized according to several properties, which are listed in Figure 2. These properties will be further defined in Sections 3 and 4.

## 3 | CONVENTIONAL QMRI RECONSTRUCTION

This section describes the mathematical formulation of conventional qMRI, introducing a notation that will be used throughout this work. qMRI reconstruction aims at the estimation of parameter maps from measured k-space data and is conventionally performed in two steps: “image reconstruction” and “parameter estimation.” To facilitate reading, a list of symbols used in this work is provided in Table A1 in the Appendix.

## 3.1 | Image reconstruction

In a multicontrast multichannel experiment with  $n^c$  contrasts indexed by  $c \in \{1, \dots, n^c\}$  and  $n^s$  coil sensitivity

maps indexed by  $s \in \{1, \dots, n^s\}$ , the measured MRI signal  $Y_{c,s}(\mathbf{v})$  at a point  $\mathbf{v} \in \Omega$ , where  $\Omega \subset \mathbb{R}^3$  denotes the three-dimensional (3D) Fourier space, also known as k-space, can be described as:

$$\tilde{Y}_{c,s}(\mathbf{v}) = \int_{\tilde{\mathbf{r}}} e^{-i2\pi\tilde{\mathbf{r}}\mathbf{v}} \tilde{C}_s(\tilde{\mathbf{r}}) \tilde{I}_c(\tilde{\mathbf{r}}) d\tilde{\mathbf{r}} + \tilde{N}_{c,s}(\mathbf{v}), \quad (1)$$

where  $\tilde{I}(\tilde{\mathbf{r}})$  represents the transverse magnetization at spatial position  $\tilde{\mathbf{r}} \in \mathbb{R}^3$  in image space,  $\tilde{C}_s(\tilde{\mathbf{r}})$  is the coil sensitivity of the  $s$ th coil at position  $\tilde{\mathbf{r}}$ , and  $\tilde{N}$  is a zero-mean complex-valued Gaussian noise contribution. Note that, since the measurements  $\tilde{Y}_{c,s}(\mathbf{v})$  are made in discrete space, the reconstruction of the continuous magnetization  $\tilde{I}(\tilde{\mathbf{r}})$  is ill-posed. In practice, however, images of the transversal magnetization are reconstructed on a finite 3D grid  $\{\mathbf{r}_j\}_1^{n_j}$  with  $\mathbf{r}_j \in \mathbb{R}^3, \forall j \in \{1, \dots, n^j\}$  where  $n^j$  denotes the number of grid points. In this case, the relationship described by Equation (1) can be approximated by a discrete Fourier Transform:

$$Y_{c,s,\mathbf{v}} = \sum_j C_{s,\mathbf{r}_j} I_{c,\mathbf{r}_j} e^{-\frac{i2\pi}{n^j} \mathbf{v}^T \mathbf{r}_j} + N_{c,s,\mathbf{v}}. \quad (2)$$

$\mathbf{Y} \in \mathbb{C}^{n^c \times n^s \times n^k}$  represents the acquired k-space points with  $n^k$  points sampled for each contrast and coil channel, indexed by  $k \in \{1, \dots, n^k\}$ ,  $\mathbf{C} \in \mathbb{C}^{n^s \times n^j}$  represents the coil sensitivity maps,  $\mathbf{I} \in \mathbb{C}^{n^c \times n^j}$  denotes the contrast images, and  $\mathbf{N} \in \mathbb{C}^{n^c \times n^s \times n^k}$  is a zero-mean, complex-valued Gaussian noise contribution. For an undersampled acquisition, the set of acquired k-space points does not satisfy the Nyquist criteria. Note that Equation (2) can be written using an encoding operator  $\mathcal{E}$  that combines the coil sensitivity maps and the (nonuniform) Fourier Transform for the sampled points:

$$\mathbf{Y} = \mathcal{E}\mathbf{I} + \mathbf{N}, \quad (3)$$

where  $\mathbf{Y}$ ,  $\mathbf{I}$ , and  $\mathbf{N}$  are (implicitly) reshaped into vectors when operators are applied. Note that the operator can be applied to both Cartesian and non-Cartesian (such as spiral or radial) sampling trajectories by only changing the set of k-space locations ( $\mathbf{v}$ ).

Conventionally, for a fully sampled multichannel acquisition, contrast images are reconstructed by applying an inverse discrete (or density compensated nonuniform) Fourier transform to the k-space data of each coil channel, followed by a combination of images corresponding to each coil channel.<sup>17</sup> Application of this technique to undersampled k-space coil data may produce aliased images. However, for suitable undersampling patterns, it is possible to reconstruct artifact-free images using an iterative approach through parallel imaging (PI)

reconstruction. To ease the notation below, we use a named index to select an element in the corresponding dimension of an object, without explicitly listing the other dimensions. So,  $\mathbf{I}_c \in \mathbb{C}^{n^j}$  is a vector with the  $n^j$  voxels in the  $c^{th}$  contrast. Assuming the image domain coil sensitivity maps are available, the PI image reconstruction, also known as SENSE,<sup>18</sup> can be formulated as follows:

$$\hat{\mathbf{I}}_c = \arg \min_{\mathbf{I}_c} \|\mathbf{Y}_c - \mathcal{E}_c \mathbf{I}_c\|_2^2. \quad (4)$$

In case the explicit coil sensitivity maps are not available, auto-calibrating PI techniques such as GRAPPA<sup>19</sup> are performed to reconstruct individual contrast images. In GRAPPA, the missing samples in undersampled k-space data are predicted using a linear combination of the acquired neighboring k-space data across all the coils. A fully sampled patch of k-space data, also known as a calibration region, is used to learn the relationship between the acquired and missing samples using reconstruction weights, known as kernels. The fully sampled k-space is then followed by the Fourier transform and a combination of images corresponding to each coil channel. The image reconstruction approaches described in this section are referred to as FTC.

### 3.2 | Parameter estimation

The second step of the conventional qMRI reconstruction approach is parameter estimation using model fitting. In this technique,  $n^q$  tissue parameter maps, represented by  $\mathbf{X} \in \mathbb{R}^{n^q \times n^j}$ , are estimated from the contrast images. Let  $\mathbf{X}_j \in \mathbb{R}^{n^q}$  represent the vector containing the tissue parameters for the  $j$ th voxel and  $\mathbf{I}_j \in \mathbb{C}^{n^c}$  is a vector that contains the values of the  $n^c$  different contrast images, referred to as signal evolution, in the  $j$ th voxel. Next, let the relationship between the contrast images and the underlying tissue parameters of interest in each voxel be modeled as:

$$\mathbf{I} = \mathcal{U}(\mathbf{X}), \quad (5)$$

with  $\mathcal{U}(\mathbf{X}) : \mathbb{R}^{n^q \times n^j} \rightarrow \mathbb{R}^{n^c \times n^j}$  a parametric function that represents a qMRI model such as a relaxometry, diffusion, or perfusion model. Note that this function will not only depend on  $\mathbf{X}$ , but also on the image acquisition settings, which are assumed to be known.

In the parameter estimation step, the tissue parameter maps  $\mathbf{X}$  can be estimated by fitting the parametric model to the reconstructed contrast images using a goodness-of-fit criterion, such as the sum of squared differences, least squares criterion, or the (penalized) likelihood function.<sup>20-23</sup> This process can be denoted by  $\mathcal{U}^{-1}$ . When



$\mathcal{U}$  evaluates each voxel independently, the tissue parameter maps can be estimated voxelwise:

$$\hat{\mathbf{X}}_j = \mathcal{U}^{-1}(\hat{\mathbf{I}}_j) = \arg \min_{\mathbf{X}_j} \|\hat{\mathbf{I}}_j - \mathcal{U}(\mathbf{X}_j)\|_2^2, \quad (6)$$

where  $\hat{\mathbf{I}}$  refers to the reconstructed images obtained in the image reconstruction step. Note that depending on the application, the parameters can be estimated from reconstructed complex-valued images (e.g., flow parameter estimation<sup>24</sup>), or reconstructed magnitude images (e.g., conventional diffusion tensor imaging<sup>25</sup>).

## 4 | RESULTS

The papers considered in this review aim at estimating parameter maps  $\mathbf{X}$  from undersampled k-space data  $\mathbf{Y}$ . These works either modify the conventional image reconstruction step (Section 3.1), the conventional parameter mapping step (Section 3.2), both, or directly estimate qMRI parameters  $\mathbf{X}$  from undersampled  $\mathbf{Y}$ . Works that include an intermediate image reconstruction step are categorized as indirect reconstruction, whereas techniques that skip the image reconstruction step and estimate parameters directly from k-space data are categorized as direct reconstruction. Both indirect and direct reconstruction are further divided into different subcategories as shown in Figure 2.

In the current section, for each subcategory, first, a theoretical overview is provided that describes the basic technique used in that subcategory. Next, the advancements proposed in the reviewed papers within this subcategory are described. Note that this is not necessarily a complete literature review on such subcategory. The complete list of the papers that were selected in the categorization phase, in combination with the properties that describe them, can be found in Table A3 in the Appendix and a more detailed version of this table with additional information on the acquisition sequence and trajectory, and optimization solvers is available [online](#).

### 4.1 | Indirect reconstruction

This category presents techniques that follow a two-step procedure of image reconstruction followed by parameter estimation.

#### 4.1.1 | Image reconstruction

This section categorizes the techniques that jointly reconstruct all the contrast images.

#### Multicontrast PI

The multicontrast PI subcategory includes PI techniques that have been extended to include multicontrast redundancy. Both image and k-space domain-based techniques have been developed and are described below:

*Image domain PI.* In SENSE reconstruction, the coil sensitivity maps can be estimated from a separate scan or a calibration region. Alternatively, studies have been performed to eliminate the need to acquire a calibration region by jointly estimating the coil sensitivity maps with the contrast images.<sup>26,27</sup> In this case, the iterative reconstruction described by Equation (4) is formulated as a nonlinear inverse problem with both  $\mathbf{I}_c$  and  $\mathbf{C}$  as unknowns. This problem has then been solved by enforcing smoothness of the coil sensitivities in a regularized reconstruction,<sup>26</sup> or using kernel calibration.<sup>27</sup> Multicontrast SENSE reconstruction can be combined with reconstruction techniques for other acceleration techniques such as simultaneous multislice imaging (SMS), where multiple slices in the field-of-view are acquired simultaneously by using multi-band RF pulses<sup>28</sup> or the “UNFOLD” method that involves sampling of different k-space points from contrast to contrast and applies filters along the contrast dimension.<sup>29</sup>

*k-space domain PI.* K-space domain-based PI techniques, such as GRAPPA, have been extended to include the prediction of missing k-space samples from data with different contrasts.<sup>30-37</sup> Additionally, GRAPPA has been applied in undersampled 3D acquisitions to reconstruct the missing k-space points along the partition encoding dimension.<sup>38</sup> Furthermore, GRAPPA has been extended to include SMS acquisitions. In this case, GRAPPA is used to unwrap the intermixed signal of the simultaneously acquired slices.<sup>39-45</sup> Finally, GRAPPA has been followed by an iterative reconstruction where distortion and noise in the reconstructed images are reduced.<sup>46</sup>

#### Regularized reconstruction

Techniques in the regularized reconstruction subcategory use prior knowledge of the sparsity in specific domains to improve image reconstruction. Regularized reconstruction can be formulated based on Bayes' theorem as a combination of the likelihood function and prior knowledge in the form of regularizer terms. Assuming the operator  $\phi$  transforms the images to be reconstructed to a desired sparse domain, then the reconstruction problem with  $n^i$  sparsifying transforms, indexed by  $i$ , can be formulated as the following optimization problem:

$$\hat{\mathbf{I}} = \arg \min_{\mathbf{I}} \|\mathbf{Y} - \mathcal{E}\mathbf{I}\|_2^2 + \sum_i^{n^i} \lambda_i \|\phi_i(\mathbf{I})\|_1, \quad (7)$$

where  $\lambda_i$  is the regularization weight of the  $i$ th sparsifying transform and  $l \in \mathbb{N}$  defines the regularization norm. Note that, the transform operator  $\phi$  can be applied across spatial as well as contrast dimensions.

**Transform domain.** Finding a suitable transform domain where the signal is sparse has been one of the challenges in performing regularized reconstruction. Different transform operators  $\phi$  and priors have been proposed to find a sparse representation of the images. This includes the wavelet transform,<sup>27,47-52</sup> the total variation transform,<sup>26,50,52-68</sup> group sparsity where images are divided into multiple sparse regions,<sup>69</sup> weighted quadratic prior that aims to suppress the noise and reconstruction artifacts based on the intensity differences between neighboring voxels,<sup>56</sup> gradient across the contrast dimension,<sup>53,70-74</sup> second-order discrete derivative in the contrast dimension,<sup>75,76</sup> principal component analysis-based transform,<sup>75,77-80</sup> image ratio constraints, where the ratio between a low-resolution image and the reconstructed image is used as a constraint,<sup>50</sup> and learned sparsifying transform  $\phi$  from the measurements.<sup>81</sup>

Apart from these, alternative ways to use regularizers and transform domains have been proposed. First, using a mixed  $l_1 - l_2$  norm through distributed compressed sensing has been proposed that promotes sparsity along the contrast and spatial dimensions simultaneously.<sup>52,82,83</sup> Secondly, priors based on the distribution of the contrast images, for example, a Gaussian process prior are proposed.<sup>84</sup> Finally, the reconstruction problem can be constrained using a parametric model:<sup>59</sup>

$$\hat{\mathbf{I}} = \arg \min_{\mathbf{I}} \|\mathbf{Y} - \mathcal{E}\mathbf{I}\|_2^2 + \gamma \|\mathbf{U}^{-1}(\mathbf{I}) - \mathbf{I}\|_1 + \lambda \|\phi(\mathbf{I})\|_l, \quad (8)$$

**Low-rank priors.** The matrix of contrast images  $\mathbf{I}$ , in which each row is a vectorized contrast image and each column shows the signal evolution for one voxel, can be assumed to be a low-rank matrix (referred to as Casorati low-rankness). Such assumptions can be incorporated as prior information by formulating the regularized reconstruction in the form of a rank constraint:

$$\hat{\mathbf{I}} = \arg \min_{\mathbf{I}} \|\mathbf{Y} - \mathcal{E}\mathbf{I}\|_2^2 + \sum_i \lambda_i \|\phi_i(\mathbf{I})\|_l + \gamma \text{rank}(\mathbf{I}), \quad (9)$$

where  $\gamma$  defines the weight of the rank constraint. However, due to the rank constraint, the optimization problem described by Equation (9) is not convex. Therefore, the nuclear norm of the matrix of contrast images  $\|\mathbf{I}\|_*$ , that is, the sum of its singular values, has been often used as convex relaxation of the rank function,<sup>61,79,80,82,85-99</sup> giving the reconstruction problem:

$$\hat{\mathbf{I}} = \arg \min_{\mathbf{I}} \|\mathbf{Y} - \mathcal{E}\mathbf{I}\|_2^2 + \sum_i \lambda_i \|\phi_i(\mathbf{I})\|_l + \gamma \|\mathbf{I}\|_*. \quad (10)$$

The nuclear norm regularization can also be applied to phase data in applications where phase correction needs to be integrated into the image reconstruction.<sup>100</sup> Instead of the nuclear norm, a log-sum relaxation form of the rank constraint based on the weighted nuclear norm minimization has been proposed to simplify the optimization of Equation (9).<sup>101</sup>

As another option, a patch-based low-rank constraint can be used.<sup>52,102-106</sup> Let  $\mathcal{P}_j$  be an operator that vectorizes a patch of contrast images around voxel  $j$ , corresponding to the selection of a set of columns of  $\mathbf{I}$ , then the reconstruction problem can be formulated as:

$$\hat{\mathbf{I}} = \arg \min_{\mathbf{I}} \|\mathbf{Y} - \mathcal{E}\mathbf{I}\|_2^2 + \gamma \sum_j \|\mathcal{P}_j \mathbf{I}\|_*. \quad (11)$$

**Combination with other techniques.** Regularized reconstruction has been used in the Generalized SLICE Dithered Enhanced Resolution technique, which is a newly developed RF encoding technique.<sup>107</sup> In this technique, the reconstruction has an extra processing step where the super-resolution reconstruction model relates the acquired thick-slice RF-encoded volumes to the desired thin-slice volumes. A joint regularized optimization is performed on the images that are initially reconstructed using k-space-based PI techniques.<sup>36,43,108</sup> Different regularizers have been used in the extra enhancement step, including the Huber function that preserves the sharp edges of the contrast images,<sup>108</sup> the Tikhonov regularizer,<sup>36</sup> and the finite difference transform.<sup>43</sup>

**Optimization algorithms.** Solving the combined optimization of data fidelity and regularizer terms can be difficult and often a more relaxed version of the cost function has been used which is computationally easier to optimize. One of the commonly used algorithms in optimization of the regularized cost functions is the Alternate Direction Method of Multipliers.<sup>52,53,57,69,93,95,100,101,103</sup> Other techniques include the gradient descent algorithm,<sup>72-74</sup> the Fast Composite Splitting Algorithm<sup>61,82</sup> and majorization-minimization-based algorithms such as the fast iterative shrinkage-thresholding algorithm.<sup>106</sup>

### Subspace constrained reconstruction

The central assumption behind papers in the subspace-constrained reconstruction subcategory is that the signal evolution across the contrasts lies in a low-dimensional subspace.<sup>109</sup> This differs from the low-rank prior introduced in Section 4.1.1.2 by explicitly, and often a priori, specifying a rank for the signal evolution subspace and often also a subspace basis. In

this case, the matrix  $\mathbf{I}$  can be approximated with a linear relationship as  $\mathbf{I} \approx \boldsymbol{\psi} \boldsymbol{\sigma}$ , with  $\boldsymbol{\psi} \in \mathbb{C}^{n^c \times n^b}$  containing the  $n^b$  basis functions, and  $\boldsymbol{\sigma} \in \mathbb{C}^{n^b \times n^j}$  their voxel-wise weights. The image reconstruction problem can then be simplified by estimating voxel-wise weights  $\boldsymbol{\sigma}$  instead of contrast images  $\mathbf{I}$  as follows:

$$\hat{\boldsymbol{\sigma}} = \arg \min_{\boldsymbol{\sigma}} \|\mathbf{Y} - \mathcal{E} \boldsymbol{\psi} \boldsymbol{\sigma}\|_2^2. \quad (12)$$

**Subspace computation.** The subspace  $\boldsymbol{\psi}$  is typically obtained by singular value decomposition of a dictionary of possible signal evolutions.

Model-based dictionaries  $\mathbf{D} \in \mathbb{C}^{n^c \times n^d}$  consist of  $n^d$  dictionary items, each with the expected signal evolution for the given acquisition settings and specific qMRI parameters.<sup>110-136</sup> More details about the generation of the dictionaries are presented in Section 4.1.2.1.

It has been shown that using patches of  $\mathbf{I}$  to create subspace functions, improves the compression of the dictionary by accounting for local similarities among signal evolutions.<sup>137-142</sup>

Furthermore, the subspace initially generated using the model-based dictionary, can be updated in an iterative reconstruction. In each iteration of this reconstruction, the subspace is updated using the reconstructed images.<sup>143-145</sup> Additionally, to better represent the nonlinearity in the signal evolution, it has been proposed to generate the subspace using kernel-based principal component analysis, in which the subspace is learned from low-resolution training data.<sup>146-148</sup>

Alternatively to dictionary generation, the subspace basis functions  $\boldsymbol{\psi}$  can be estimated along with the voxel-wise weights  $\boldsymbol{\sigma}$  during the reconstruction step by using the “blind compressed sensing” principle.<sup>149</sup>

$$\{\hat{\boldsymbol{\psi}}, \hat{\boldsymbol{\sigma}}\} = \arg \min_{\boldsymbol{\psi}, \boldsymbol{\sigma}} \|\mathbf{Y} - \mathcal{E} \boldsymbol{\psi} \boldsymbol{\sigma}\|_F^2 + \lambda \|\boldsymbol{\sigma}\|_1 \quad (13)$$

such that  $\|\boldsymbol{\psi}\|_F^2 < 1$ ,

where  $\|\boldsymbol{\psi}\|_F^2 < 1$  represents a unit Frobenius norm applied to make the optimization problem well-posed. The optimization (13) can be solved using a variable splitting and augmented Lagrangian optimization scheme.<sup>149</sup>

**Multiple subspace basis functions.** During data acquisition, subject motion, including rigid, respiratory, and cardiac motion, can influence the acquired signal. To account for subject motion, some techniques based on partially separable functions have been proposed. In these techniques, different subspace basis functions related to the contrasts and motion can be separately designed and used during the reconstruction.<sup>145,150-156</sup> Specifically, the contrast images  $\mathbf{I}$  can be decomposed into multiple tensors using a higher-order singular value decomposition, such

as the Tucker decomposition. For instance,  $\mathbf{I}$  is separated into components representing the signal evolution across contrasts  $\check{\boldsymbol{\psi}}$ , and motion  $\boldsymbol{\Gamma}$  as:

$$I_{c,m,j} = \sum_{b_1=1}^{n^{b_1}} \sum_{b_2=1}^{n^{b_2}} \check{\psi}_{c,b_1} \Gamma_{m,b_2} \check{\sigma}_{b_1,b_2,j}, \quad (14)$$

where  $m$  is the index for the motion states,  $b_1$  and  $b_2$  indices the basis functions of  $\check{\boldsymbol{\psi}} \in \mathbb{C}^{n^c \times n^{b_1}}$  and  $\boldsymbol{\Gamma} \in \mathbb{C}^{n^m \times n^{b_2}}$ , respectively, and  $\check{\boldsymbol{\sigma}} \in \mathbb{C}^{n^{b_1} \times n^{b_2} \times n^j}$  represents a tensor that contains spatial weights for each basis.<sup>145,151,156,157</sup> During the reconstruction the spatial weights  $\check{\boldsymbol{\sigma}}$  are estimated. Equation (14) is limited to two bases but this number can be increased to include more aspects of the signal evolution.<sup>130,152,158-161</sup> By including SMS in the acquisition protocol, the scan time for such techniques can be further reduced.<sup>160</sup> Along similar lines, it has been proposed to separate the spatial weight  $\sigma$  into a magnitude and a unit phase component that represents the phase variations. These weights are then estimated using a block coordinate descent method.<sup>162</sup>

**Additional steps to address other aspects of the acquisition.** First, subspace constrained reconstruction has been modified to correct for phase evolution across the readout jointly with image subspace reconstruction.<sup>136,163</sup> Secondly, it has been used for compensation of B0 inhomogeneities in echo planar time imaging sequences.<sup>116</sup> Finally, it has been proposed to separate fat and water in subspace constrained reconstruction.<sup>117,138</sup>

**Additional prior in the form of a Regularizer.** Regularizers can be introduced to add prior information, such as sparsity,<sup>164</sup> to the optimization problem defined in Equation (12), yielding:

$$\hat{\boldsymbol{\sigma}} = \arg \min_{\boldsymbol{\sigma}} \|\mathbf{Y} - \mathcal{E} \boldsymbol{\psi} \boldsymbol{\sigma}\|_2^2 + \sum_i \lambda_i \|\phi_i(\boldsymbol{\sigma})\|_l. \quad (15)$$

Subspace constrained reconstruction has been used jointly with a spatially sparse representation of  $\boldsymbol{\sigma}$  using the wavelet transform,<sup>110-112,119,120,163</sup> total variation,<sup>117,119,123,124,129,143,145,155,162,165</sup> finite difference,<sup>164</sup> Fourier representation of images in the temporal direction,<sup>165</sup> low-rank priors,<sup>112,115,126,128,135-139,141,142,145,166-172</sup> and deep learning priors.<sup>173</sup>

**Alternative ways to exploit the low-rank nature of the signal.** The low-rank nature and sparsity of the signal evolution can be exploited by assuming it can be decomposed into its low-rank component  $\mathbb{L}$  and sparse component  $\mathbb{S}$ , that is,  $\mathbf{I} = \mathbb{L} + \mathbb{S}$ .<sup>60,174-178</sup> This results in the reconstruction problem:

$$\hat{\mathbb{L}}, \hat{\mathbb{S}} = \arg \min_{\mathbb{L}, \mathbb{S}} \|\mathbf{Y} - \mathcal{E}(\mathbb{L} + \mathbb{S})\|_2^2 + \lambda \|\phi(\mathbb{S})\|_l + \gamma \|\mathbb{L}\|_*. \quad (16)$$

The low-rank subspace of the signal has been used to fill the missing k-space samples.<sup>113,179-185</sup> Specifically, the subspace  $\Psi$  constructed in the image domain can be used to fill in missing k-space samples.<sup>113</sup> The k-space data can also be transformed into structured matrices, for example, block-Hankel<sup>181,182,184-186</sup> and Toeplitz,<sup>183,187</sup> to exploit the low-rank properties. In this case, the optimization problem can be rewritten as:

$$\hat{\mathbf{I}} = \arg \min_{\mathbf{I}} \|\mathbf{Y} - \mathcal{E}\mathbf{I}\|_2^2 + \sum_i^{n^i} \lambda_i \|\phi_i(\mathbf{I})\|_l + \gamma \|\mathbf{S}\mathbf{I}\|_*, \quad (17)$$

where  $\mathbf{S}$  is an operator that first converts the contrast images into the Fourier domain and then into a structured matrix such as block-Hankel, or Toeplitz. The reconstruction problem has been originally posed with a minimization constraint on  $\mathbf{S}\mathbf{I}$ ,  $\min \text{rank}[\mathbf{S}\mathbf{I}]$ , however, since this is an NP-hard problem, it is replaced with a Schatten-p quasi norm ( $0 \leq l < 1$ )<sup>187</sup> or the nuclear norm.<sup>181</sup>

It should be noted that reconstruction techniques based on structured low-rank matrices are computationally demanding due to the large size of the structured matrices. To address this issue, a more computationally efficient implementation of these techniques based on modified iterative reweighted least squares has been proposed.<sup>180</sup> To improve the reconstruction further, after solving the reconstruction problem described in Equation (17), a convolutional neural network with a U-NET architecture has been used.<sup>181,188</sup>

Another way to exploit the low-rank nature of the contrast images is by adding a regularization term penalizing the distance of the images to the subspace.<sup>47,62,63,189-194</sup> In this case, the optimization problem can be defined as:

$$\{\hat{\mathbf{I}}, \hat{\boldsymbol{\sigma}}\} = \arg \min_{\mathbf{I}, \boldsymbol{\sigma}} \|\mathbf{Y} - \mathcal{E}\mathbf{I}\|_2^2 + \gamma \|\boldsymbol{\Psi}\boldsymbol{\sigma} - \mathbf{I}\|_2^2 + \sum_i^{n^i} \lambda_i \|\phi_i(\mathbf{I})\|_l. \quad (18)$$

**Optimization algorithms.** Most of the works use alternate direction method of multipliers with variable splitting for solving subspace constrained reconstruction problems.<sup>112,115,116,118,121,122,126,128,130,139-142,144,149,162-166,169,183,187</sup>

Other solvers include the nonlinear conjugate gradient descent with backtracking line search,<sup>120</sup> the orthogonal matching pursuit method,<sup>143,190</sup> the linear conjugate gradient algorithm<sup>123</sup> and the fast iterative shrinkage-thresholding algorithm.<sup>135</sup>

#### View-sharing reconstruction

Acquisition protocols have been proposed that create densely sampled k-space frames by combining the sampled points of different subsampled contrasts. While

reconstruction of the individual contrast images from their corresponding subsampled k-space data results in aliased or low-resolution images, a smart combination of the multicontrast k-space data can reduce these issues. However, combining k-space points of different contrasts in one k-space may lead to artifacts in image space due to the difference in contrast across the k-space. Thus, additional steps, such as filtering, may be required.<sup>195</sup>

**View-sharing with shared high spatial frequency information.** The principle behind techniques in this subcategory is that the changes in the acquisition of one contrast to the other mainly affect the low spatial frequencies in the central k-space regions. Therefore, while the central regions are fully sampled for every contrast, the noncentral regions, containing the high spatial frequencies, are under-sampled. For each contrast, a k-space frame is formed by complementing the fully sampled central region with high-frequency data of multiple contrasts, after which these k-space frames are reconstructed into images.<sup>196-202</sup>

The techniques in the view-sharing subcategory have been further improved by applying additional filters to help maintaining the desired information. For instance, “k-space weighted image contrast” filters are used that help reducing streaking artifacts in radial sampling acquisitions.<sup>199-202</sup> Similarly, the application of multiple radial mask filters is examined that exploit the low spatial-frequency nature of image-to-image contrast changes.<sup>195</sup>

**View-sharing with information shared across similar contrasts.** Techniques in the view-sharing subcategory can also assume a slow variation among the contrasts such that the data from several similar contrasts can be combined into a single k-space and reconstructed into a single weighted image, thereby ignoring the contrast variations.<sup>203-210</sup> However, additional correction steps are required to reduce the effect of the small differences between the contrasts. Specifically, the trajectory or the order in which the k-space is sampled can be crucial to avoid artifacts.<sup>203</sup> View-sharing can be combined with other reconstruction techniques such as regularized reconstruction,<sup>66</sup> subspace constrained reconstruction,<sup>211</sup> or PI reconstruction.<sup>41,206,210</sup>

#### Learning-based reconstruction

Techniques in the learning-based reconstruction subcategory use neural networks that learn to reconstruct artifact-free images. In this section, we focus on the works that exploit the redundant information in contrast images in the training process of the neural network. Learning-based image reconstruction is often seen as an artifact removal step where the input of the network is the aliased images that are reconstructed using the FFC techniques as described in Section 3.1 and the output



is the artifact-free reconstructed contrast images. A neural network  $\mathcal{H}(\tilde{\mathbf{Z}}|\theta)$ , which is parameterized by  $\theta$ , is provided with aliased contrast images  $\tilde{\mathbf{Z}}$  as input, to provide artifact-free contrast images  $\hat{\mathbf{I}}$  as output:<sup>212-214</sup>

$$\hat{\mathbf{I}} = \mathcal{H}(\tilde{\mathbf{Z}}|\theta). \quad (19)$$

The parameters of the network  $\theta$  are defined in a training process, prior to image reconstruction, that can be described as:

$$\hat{\theta} = \arg \min_{\theta} \sum_t \mathcal{L}(\mathbf{W}_t, \mathcal{H}(\mathbf{Z}_t|\theta)), \quad (20)$$

where  $\mathcal{L}$  denotes a suitable loss function,  $\mathbf{W}_t$  and  $\mathbf{Z}_t$  denote the training datasets indexed by  $t \in \{1, 2, \dots, n^t\}$  with  $n^t$  the number of training datasets, where  $\mathbf{Z}_t$  corresponds to the aliased training images as input of the network and  $\mathbf{W}_t$  can correspond to both fully sampled training images or fully sampled training k-space data, depending on the application.<sup>215</sup> As an example, a model-based loss function based on the sum of squared differences where training is performed using fully sampled k-space data<sup>215</sup> can be incorporated as follows:

$$\hat{\theta} = \arg \min_{\theta} \sum_t \|\mathbf{W}_t - \mathcal{H}(\mathbf{Z}_t|\theta)\|_2^2. \quad (21)$$

The neural network can be included in an iterative reconstruction.<sup>188,216-218</sup> In this case, the optimization problem described by Equation (7) is modified such that the regularizer term includes a generative neural network as follows:

$$\hat{\mathbf{I}} = \arg \min_{\mathbf{I}} \|\mathbf{Y} - \mathcal{E}\mathbf{I}\|_2^2 + \lambda \|\mathcal{H}(\tilde{\mathbf{Z}}|\theta) - \mathbf{I}\|_1. \quad (22)$$

The neural network can be trained on previously acquired datasets,<sup>219,220</sup> on synthetic datasets,<sup>221</sup> on a combination of synthetic and real datasets,<sup>214</sup> or on a dictionary generated by a biophysical signal model.<sup>216,217</sup> The training process can be performed on image patches instead of full field-of-view images,<sup>222</sup> which allows the design of a good-performing neural network even with a small amount of training data. Also, self-supervised learning-based techniques that do not require fully sampled data have been proposed.<sup>213</sup>

The input data are often comprised of magnitude images.<sup>181,215,222,223</sup> However, in applications where the phase information is important for the subsequent parameter estimation step, complex neural networks have been developed that exploit the correlation between the real and imaginary parts of a complex image by processing the real and imaginary images with complex convolutions inspired by the multiplication of complex numbers.<sup>219</sup>

Various architectures have been investigated for the neural network, including U-NET,<sup>215,224</sup> fully connected convolutional neural network,<sup>223,225</sup> multiscale residual network,<sup>222</sup> deep cascade of residual dense network,<sup>221</sup> and deep complex residual network.<sup>219</sup>

#### 4.1.2 | Parameter estimation

The second step of the indirect reconstruction is parameter estimation. Papers that target to improve this step are categorized in this subsection. Apart from the conventional model-based technique introduced in Section 3, the parameter maps  $\mathbf{X}$  can be estimated from the reconstructed contrast images  $\hat{\mathbf{I}}$  using dictionary matching and learning-based estimation.

##### Dictionary matching

In techniques in the dictionary matching sub-category, a model-based dictionary  $\mathbf{D} \in \mathbb{C}^{n^c \times n^d}$  is generated that relates parameter values for specific scan settings to the signal evolution using the analytical model  $\mathcal{U}$ . In a qMRI experiment with  $n^q$  parameters to be estimated, the range of possible values for each parameter can be digitized with a particular number of steps and step size. If the parameters indexed by  $q \in \{1, \dots, n^q\}$  have ranges that are divided into  $n^{d_1}, \dots, n^{d_q}$  steps, then the number of steps for all the parameters included in the dictionary is  $n^d = \prod_q n^{d_q}$ . Note that  $n^d$  is also the number of expected signal evolutions defined in a dictionary.  $\mathbf{D}_d$  is the signal evolution for one set of parameters and is referred to as a dictionary atom. The size of the dictionary scales exponentially with the number of qMRI parameters  $n^q$ , which affects the computational cost of generation and usage of the dictionary. Hence, dictionaries are often generated with a small number of parameters, with a typical maximum of four.<sup>226</sup>

Matching the qMRI parameters to the measured signal (pattern matching) can be performed by solving the optimization problem described by:

$$\hat{d} = \arg \min_d \mathcal{M}(\hat{\mathbf{I}}_j, \mathbf{D}_d), \quad (23)$$

where  $\mathcal{M}$  is a function that computes the difference between the reconstructed signal and the simulated signal in the dictionary in each voxel. The set of parameters corresponding with the  $\hat{d}$ th column of the dictionary are the estimated qMRI parameters in the  $j$ th voxel.

For dictionary matching,  $\mathcal{U}$  only needs to be evaluated once to create  $\mathbf{D}$  for given acquisition settings. Various advanced simulation techniques have been used to implement  $\mathcal{U}$ , such as Bloch simulations,<sup>40,66,119-121,137,141,144,226-236</sup> extended phase

graphs,<sup>65,102,103,112,142,167,184,196,197,205,208,211,237-239</sup> and methods using advanced biophysical models of the tissue.<sup>138,192,207,240</sup>

**Auxiliary parameter estimation.** The estimation of qMRI parameters can be improved if the effects of scanner-related parameters, such as  $B_0$  and  $B_1$  field inhomogeneities, are included in the dictionary generation. Such parameters are referred to as “auxiliary parameters” in this work. To include auxiliary parameters in the dictionary generation, the dictionary needs to be extended. Such extensions may include slice profile effects,<sup>102,112,119,120,197,230</sup>  $B_1$  inhomogeneity,<sup>36,66,165,197,228-230,241-243</sup> receiver phase,<sup>230</sup>  $B_0$  inhomogeneity,<sup>40,233,244</sup> relaxation effects during the inversion and preparation pulses,<sup>120</sup> and partial volume effects.<sup>227</sup>

**Dictionary compression.** The precomputed dictionary for dictionary matching often has a considerable size and can be compressed to facilitate its implementation and reduce the required number of comparisons. Such compression has been performed using different techniques and in different dimensions. For instance, singular value decomposition,<sup>88,89,137,169,211,218,228,229,245</sup> randomized singular value decomposition,<sup>231,244</sup> and group matching<sup>246</sup> are used to compress the dictionary in the contrast dimension. Similarly, the step size for generating different parameters in the dictionary can be increased, resulting in a coarser dictionary with lower computational costs. This approach is often combined with interpolation techniques, such as quadratic interpolation<sup>244</sup> or B-spline interpolation<sup>230</sup> of dictionary entries to reduce possible artifacts. Specifically, an automatic technique is proposed to determine the dictionary resolution corresponding to a specified interpolation error.<sup>230</sup>

**Pattern matching.** Some studies focus on improving the efficiency of the dictionary matching step. For instance, the iterative brute-force searches are replaced with fast approximate nearest neighbor searches based on cover tree structures.<sup>131</sup> The gradient descent search algorithm,<sup>245</sup> and a learned Mahalanobis distance<sup>233</sup> are used for finding the closest match with dictionary entries. The robustness of results with respect to flow artifacts and intravoxel dephasing is improved by applying matching in multiple steps.<sup>228</sup>

**Combination with other techniques.** Further improvements to techniques in the dictionary matching subcategory include modifying the dictionary to make it applicable in combination with other qMRI reconstruction and acquisition techniques. For instance, a combination of view-sharing reconstruction and dictionary matching requires  $\mathbf{D}$  to be modified to account for the mixed contrast in the data.<sup>205</sup>

Dictionary matching is also used in conjunction with SMS acquisition to cover a given volume faster.

Reconstruction from SMS data requires the signal of each slice to be unfolded. Next, the unfolded signal of each slice is matched to a precomputed dictionary.<sup>40</sup> However, if the acquisition settings vary across slices, the dictionary needs to be modified accordingly, and a separate dictionary for each slice needs to be generated.<sup>232</sup>

Furthermore, dictionary matching can be followed by application of a convolutional neural network to reduce motion-induced artifacts.<sup>134</sup>

### Learning-based estimation

Learning-based estimation techniques use neural networks that learn an approximation of the inverse of the qMRI model function  $\mathcal{U}$  described in Section 3.2 to reconstruct high-quality parameter maps from (often) aliased and noisy contrast images that are reconstructed in the image reconstruction step (cf. Section 3.1). A neural network  $\mathcal{H}(\tilde{\mathbf{Z}}|\theta)$  is used where the estimated parameter maps are the output of the neural network:  $\hat{\mathbf{X}} = \mathcal{H}(\tilde{\mathbf{Z}}|\theta)$ .<sup>38,42,85,132,178,209,224,247-259</sup>

The network training procedure is similar to Equation (20) but with  $\mathbf{Z}_t$  as the set of (aliased) training images and  $\mathbf{W}_t$  denoting the artifact-free training parameter maps.

Various loss functions have been proposed to improve the performance of the neural network. For instance, the loss function is defined as the squared error of each estimate normalized by the corresponding Cramér–Rao bound (CRB) before averaging all the estimated parameters and all the samples in the training data.<sup>170</sup> Such a loss function that includes the CRB allows the network to account for variations in the noise propagation among the parameters.<sup>170</sup> Similarly, a total variation regularizer along with the mean squared error is used as a loss function,<sup>258</sup> which results in smooth reconstructed parameter maps.

Complex-valued contrast images have been used for training and testing the neural network, showing a high fidelity of parameter quantification.<sup>133,260</sup> Learning-based parameter estimation can be improved by joint estimation of the  $B_1$  field map along with the relaxometry parameters.<sup>223,261</sup>

Learning-based techniques relying on random-forest regression<sup>45</sup> and regression with kernels<sup>262</sup> have been proposed to estimate artifact-free quantitative parameter maps from the reconstructed contrast images which can have undersampling artifacts. Furthermore, deep learning frameworks have been applied to accelerate parameter estimation, particularly when many parameters need to be estimated.<sup>263</sup> It has been proposed to use attention-based neural networks to address the need for explainable architectures in neural networks used for parameter matching.<sup>264</sup>

## 4.2 | Direct reconstruction

Techniques in this category skip the image reconstruction step and directly estimate  $\mathbf{X}$  from undersampled  $\mathbf{Y}$ , usually through an iterative process. They can be categorized in two subcategories.

### 4.2.1 | Direct model-based reconstruction

The techniques in the direct model-based reconstruction subcategory exploit the redundancies in the data by incorporating a physical signal model  $\mathcal{U}$  in the reconstruction.<sup>265-269</sup> The basic formulation for direct model-based reconstruction is given by:

$$\hat{\mathbf{X}} = \arg \min_{\mathbf{X}} \|\mathbf{Y} - \mathcal{E}\mathcal{U}(\mathbf{X})\|_2^2. \quad (24)$$

*Adjustment of the physical signal model.* The signal model  $\mathcal{U}$  can be adjusted to improve parameter estimation. The related studies are often focused on:

- Developing signal models that more accurately describe the tissue characteristics and acquisition settings, such as the inversion recovery Look-Locker model for  $T_1$  mapping,<sup>270</sup> the variable flip angle model for  $T_1$  mapping,<sup>271</sup> the chemical shift model for water-fat separation imaging,<sup>272</sup> the echo-modulation curve model for  $T_2$  mapping,<sup>267</sup> the Kalman filter model for  $T_2$  mapping,<sup>273</sup> the generating function formalism for  $T_2$  mapping,<sup>274</sup> and models based on Bloch equations for direct estimation of parameters from transient response signals.<sup>275-278</sup>
- Developing novel models that parameterize the model jointly for auxiliary parameters. For instance: the joint estimation of off-resonance frequency in  $T_2^*$  mapping,<sup>279</sup> the joint estimation of  $T_2^*$  and field maps in water and fat parameter estimation,<sup>272,280,281</sup> the joint estimation of flip angles and proton density maps in  $T_2$  mapping,<sup>282</sup> the joint estimation of steady-state signal, equilibrium signal, and effective relaxation rate in  $T_1$  mapping,<sup>283-285</sup> the joint estimation of tracer kinetic model parameters in  $T_1$  mapping,<sup>286</sup> and the joint estimation of phase parameters in multishot diffusion imaging.<sup>287,288</sup>

*Regularized direct reconstruction.* To improve the performance of direct reconstruction, prior information about the qMRI parameters to be estimated can be incorporated by adding regularization terms, such as Tikhonov regularizer,<sup>274</sup>  $l_1$  norm regularizer,<sup>289</sup> and weighted  $l_1$  ball regularizer<sup>268,290</sup> to the cost function described by Equation (24). These priors can promote the sparsity

of the parameter maps in different transform domains, such as total variation transform,<sup>269,286,291-294</sup> the wavelet transforms,<sup>281,283-285,295-298</sup> the total generalized variation transform,<sup>299</sup> the fractional variation constraint,<sup>282</sup> the surfacelet transform,<sup>300,301</sup> patch-based difference operator,<sup>302</sup> and the finite difference transform.<sup>303</sup>

In these cases, the optimization problem (24) is modified to include regularizer terms yielding

$$\hat{\mathbf{X}} = \arg \min_{\mathbf{X}} \|\mathbf{Y} - \mathcal{E}\mathcal{U}(\mathbf{X})\|_2^2 + \sum_i^{n_i} \lambda_i \|\phi_i(\mathbf{X})\|_l. \quad (25)$$

Furthermore, it has been proposed to jointly estimate the coil sensitivity maps along with the qMRI parameters in direct reconstruction, where a Sobolev norm is applied to these maps to enforce smoothness.<sup>284,285,296</sup> Additionally, to enforce phase smoothness in the joint reconstruction of phase and qMRI parameters, application of an  $l_2$  norm regularization on the spatial gradient of the phase maps has been proposed.<sup>294</sup>

*Joint image reconstruction and parameter estimation.* In some applications, parameter maps are estimated jointly with the images:<sup>304,305</sup>

$$\hat{\mathbf{X}}, \hat{\mathbf{I}} = \arg \min_{\mathbf{X}, \mathbf{I}} \|\mathbf{I} - \mathcal{U}(\mathbf{X})\|_2^2 + \|\mathbf{Y} - \mathcal{E}\mathcal{U}(\mathbf{X})\|_2^2 + \lambda_1 \|\phi_1(\mathbf{I})\|_l + \lambda_2 \|\phi_2(\mathbf{X})\|_l. \quad (26)$$

Estimating both contrast images and parameter maps allows the application of prior information in both the parameter and image domains. To promote local coherence of contrast images, it has been proposed to apply a low-rank prior on contrast images using a nuclear norm regularizer term in direct reconstruction.<sup>286</sup>

*Combination with other techniques.* Techniques in the direct model-based reconstruction subcategory have been combined with other qMRI reconstruction techniques. High acceleration rates have been achieved by a combination of direct reconstruction of  $T_2$  maps with PI techniques where the first echo in a multi-echo gradient echo scans is used for GRAPPA calibration.<sup>306</sup> The combination of direct reconstruction and PI allows for exploiting the prior knowledge from both local k-space dependencies and the physical signal model, which has been investigated in various organs in human body.<sup>306-308</sup> Furthermore, direct reconstruction has been combined with SMS acquisitions, by incorporating the SMS encoding matrix into the encoding operator  $\mathcal{E}$ .<sup>285</sup>

*Optimization algorithms.* Minimizing the cost function of a direct model-based reconstruction problem is often challenging as it involves a nonlinear optimization problem. To solve this problem, exponential models can be approximated with their Taylor series

expansion<sup>281,302</sup> or linearized in a small neighborhood using the Gauss–Newton approach.<sup>299</sup> Additionally, the nonlinear optimization problem can be treated as a tomography problem and solved using large-scale nonlinear optimization routines.<sup>278,309</sup> The computational time of techniques in direct reconstruction can be decreased using block-wise decomposition of the cost function in combination with a specific uniform under-sampling pattern.<sup>310</sup> In case multiparametric models are used, advanced solvers such as Stochastic Gradient Langevin dynamics,<sup>286</sup> regularized trust region continuation techniques,<sup>279</sup> or alternating minimization<sup>288,295</sup> have been proposed to optimize the nonlinear cost-function jointly for different parameters. Furthermore, it has been proposed to automatically scale the unknown parameters in the joint optimization, which numerically balances the partial derivatives of the multiparametric model to improve the conditioning and hence ease the optimization.<sup>311</sup>

#### 4.2.2 | Direct learning-based reconstruction

Techniques in the direct learning-based reconstruction subcategory aim to replace the direct model-based reconstruction with a neural network to estimate qMRI parameter maps directly from the acquired k-space data. The neural network  $\mathcal{H}$  has undersampled k-space data as input, that is,  $\tilde{\mathbf{Z}} = \mathbf{Y}$  and estimated qMRI parameter maps as output, that is,  $\hat{\mathbf{X}} = \mathcal{H}(\tilde{\mathbf{Z}}|\theta)$ . The training process for optimizing network parameters  $\theta$  is similar to Equation (20), with  $\mathbf{W}_i$  and  $\mathbf{Z}_i$  denoting the reference parameter maps and undersampled k-space data of a training dataset, respectively.

The computational costs of training a neural network that performs direct estimation of parameter maps from k-space data are high. Therefore, alternatively, neural networks have been proposed to improve parts of the techniques in the direct model-based reconstruction approach.<sup>312–316</sup> For instance, deep learning networks have been designed to regularize the estimation of parameter maps in Equation (24).<sup>312–314</sup> Similarly, neural networks have been proposed to estimate the initial parameter maps of the direct model-based reconstruction from undersampled k-space data.<sup>314</sup> Further, it has been proposed to predict the derivatives of a direct forward model using a pretrained neural network, decreasing the computation time for direct model-based reconstruction.<sup>315</sup>

Finally, a self-supervised learning-based approach has been proposed to perform real-time parameter mapping for transient imaging.<sup>316</sup> In this approach, the Fourier Transform of the parameter maps is computed from the undersampled k-space data, after which parameter maps are obtained by Fourier Transform.

## 5 | RESULTS: GRAPHICAL REPRESENTATION

The current section presents figures that visualize the distribution of the 292 reviewed papers over different categories. Figure 3A shows that 240 papers were categorized as indirect reconstruction, whereas the remaining 52 papers were categorized as direct reconstruction. Figure 3B shows a further subcategorization of the indirect reconstruction category, classifying the papers based on their image reconstruction step (top) and parameter estimation step (bottom). Note that the subcategories FTC

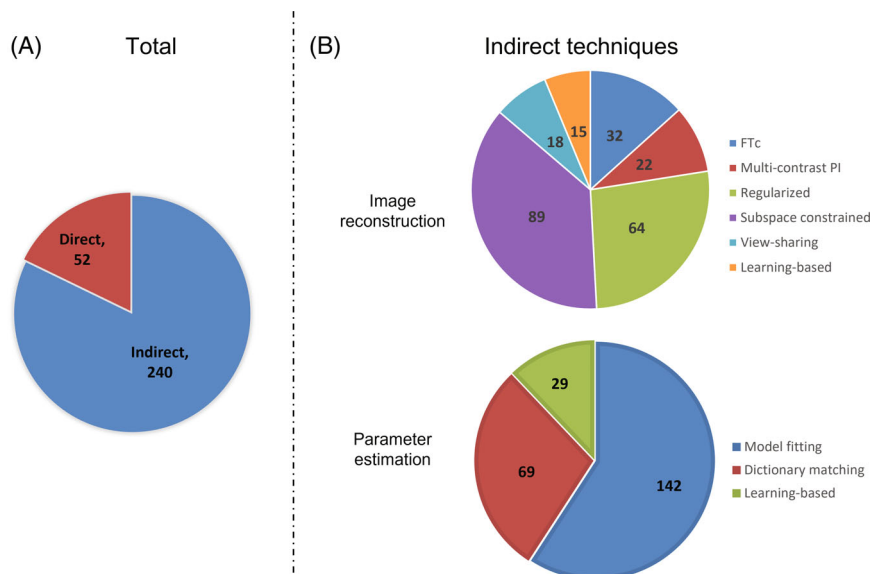


**FIGURE 3** Distribution of articles included in the review: (A) direct versus indirect categories; (B) Image reconstruction (top) and parameter estimation (bottom) within the indirect category.



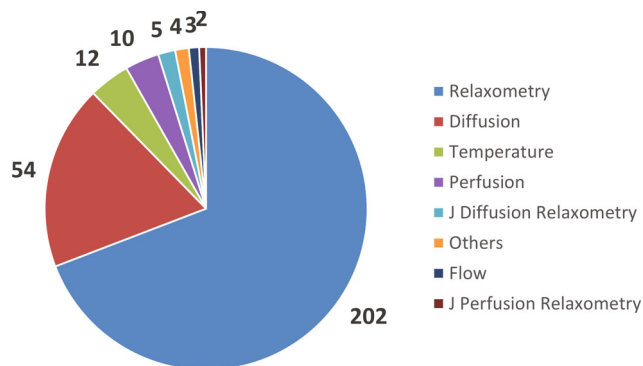


**FIGURE 4** The distribution of articles included in this review over the different classes of target quantitative magnetic resonance imaging parameters. The letter J in front of the parameter indicates joint estimation of multiple quantitative parameters.

(top) and model fitting (bottom) correspond with the conventional image reconstruction and parameter estimation step of a classical two-step approach, respectively. Obviously, no paper selected in this review classifies for both these subcategories, since the inclusion criteria require a modification of at least one step of the conventional two-step approach.

Figure 4 shows the distribution of the articles over the following classes of target qMRI parameters:

1. **Relaxometry** which includes  $T_1$ ,  $T_1\rho$ ,  $T_{1H_2O}$ ,  $T_2$ ,  $T_2^*$ , proton density, spin density, magnetization transfer, myelin water fraction, quantitative susceptibility mapping, fat fraction, and water fraction.
2. **Diffusion** which includes apparent diffusion coefficients, mean diffusivity, fractional anisotropy, and parameters of more advanced diffusion models that are mentioned in the table available [online](#).
3. **Temperature** based on proton resonance frequency shift.

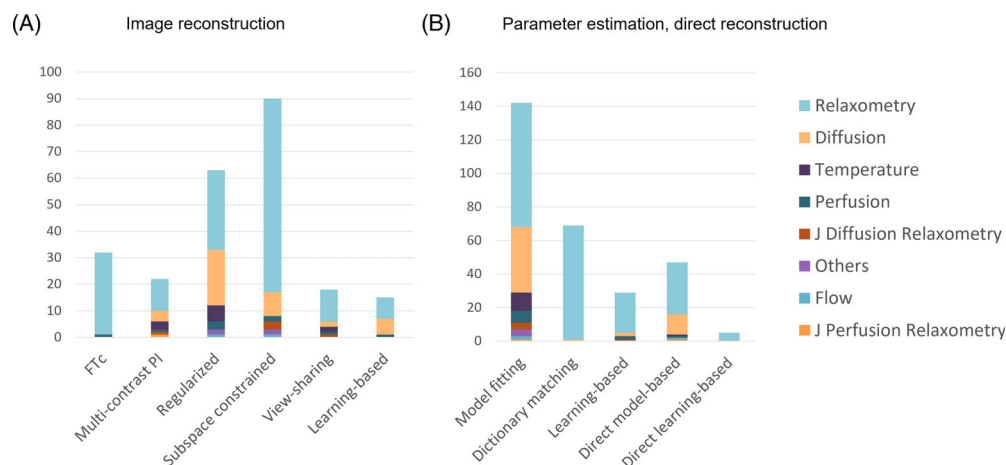
4. **Perfusion** which includes parameters of arterial spin labeling and tracer-kinetic models.
5. **Flow** based on velocity mapping.
6. **Others** which consists of Hyperpolarized  $^{13}\text{C}$ , tissue sodium concentration, and Paramagnetic fluorine-19 parameters.

Figure 4 shows that about 70% of the papers reviewed in this work focus on relaxometry.

Figure 5 shows the number of papers reviewed in this work that consider a specific category of target parameters while presenting a novelty that can be categorized to one of the image reconstruction subcategories (Figure 5A), parameter estimation subcategories (Figure 5B) or direct techniques subcategories (Figure 5B) that were described in Section 3 and 4 and summarized in Figure 2.

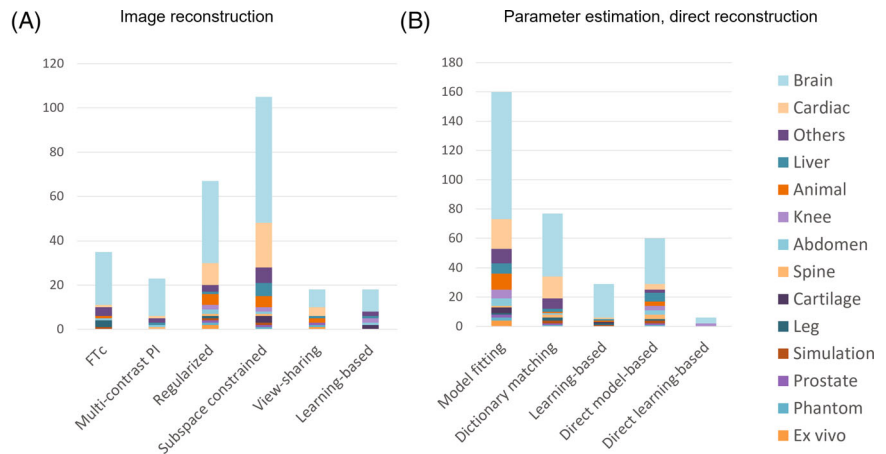
Similarly, Figure 6 shows the number of papers that target a specific application domain while presenting a novelty that can be categorized to one of the image reconstruction subcategories (Figure 6A), parameter estimation subcategories (Figure 6B), or direct techniques subcategories (Figure 6B). It can be observed from Figure 6 that the main application domain is brain MRI, while lung MRI (not specified, but included in the category “others”) is the least covered.

Figure 7 demonstrates the distribution of articles over the publication year. It can be seen that 167 out of the 292 reviewed papers were published from 2019 to 2022. After 2012, the variety of targeted parameters (Figure 7A) and the application domains (Figure 7B) increased. Furthermore, it can be observed in Figure 7C,D that the learning-based techniques started to be used in parameter estimation in 2017 and in image reconstruction in 2019. Figure 7E shows the number of articles that included a public link to the acquired datasets or the implemented code, in different years. The individual links are available in Table 3 and are summarized in this [GitBook](#) page.



**FIGURE 5** The number of articles that consider a specific class of target parameters, while presenting a novelty that can be categorized to one of the image reconstruction subcategories (A), parameter estimation subcategories (B), or direct reconstruction subcategories (B). The letter J in front of the parameter indicates joint estimation of multiple quantitative parameters.

**FIGURE 6** The number of articles that consider a specific application domain, while presenting a novelty that can be categorized to one of the image reconstruction subcategories (A), parameter estimation subcategories (B), or direct reconstruction subcategories (B).



## 6 | DISCUSSION

This work describes and categorizes the different reconstruction techniques used for undersampled qMRI acquisitions in a unified mathematical framework, focusing on their methodological contribution while ignoring case-specific variables. Accelerated qMRI methods have enabled for example  $T_1$  and  $T_2$  mapping of the whole brain with  $1 \text{ mm}^3$  resolution in just 3 min<sup>126,152</sup> and cardiac  $T_1$  and  $T_2$  mapping with a single breath-hold scan in about 16 s.<sup>141</sup>

Accelerated qMRI is an active, fast-growing research field, a trend supported by the observation that around half of the papers included in this work were published in the last 3 years. The growing number of publications and the emergence of new methodologies, such as learning-based techniques, indicate the interest of the research community in further acceleration of qMRI as well as in more accurate and trustworthy techniques. Figure 7E, shows an increasing trend in the number of articles with publicly available code or data, suggesting improvements in transparent developments and collaborations.

The distribution of articles over the years suggests a gradually increasing application of all techniques. However, a jump can be observed in 2016 for FTC and multicontrast PI subcategories in image reconstruction and for dictionary matching subcategory in parameter estimation. This jump can be related to the emergence of transient response multi-parametric imaging techniques<sup>236</sup> that often reconstruct the contrast images using FTC and PI techniques and remove the undersampling artifacts in the parameter estimation step using dictionary matching.

The distribution over target parameters that can be observed in Figure 7A shows an inclination toward investigating relaxometry. The reasons contributing to this could be the large variety and accessibility of relaxometry imaging sequences, and the wider availability of

relaxation phantoms compared to other parameters. Other modalities, such as diffusion MRI, result in contrast images with lower signal-to-noise ratio values compared to relaxometry imaging, which creates a need for more data samples.<sup>317</sup> In perfusion imaging, in addition to the problem of low signal-to-noise ratio, there is a lack of a gold standard for validating the results, as designing a perfusion phantom is challenging.<sup>318</sup> These reasons can contribute to making relaxometry a better candidate for undersampled acquisitions.

The brain is the most investigated application domain for qMRI techniques. With the many properties that MRI can measure, it is uniquely positioned to study the complex composition and abnormalities in the brain. With the relative absence of motion and other disturbing factors, combined with strong interest from the neurological and neuroscience communities, it is logical that many techniques are first proposed for brain imaging. Next to the brain, cardiac applications are highly investigated with accelerated qMRI techniques. qMRI enhances the knowledge of cardiac function, volume, and tissue characterization. It allows for the spatial visualization of changes in the myocardium based on changes in myocardial relaxation times and flows, enabling the evaluation of diffuse changes within the myocardium. In this way, cardiac qMRI facilitates exploring the link between biology and the clinical manifestation of cardiac diseases and is an important imaging modality. However, cardiac imaging is more challenging than brain imaging due to substantial non-rigid motion during the scan, which is unavoidable during the long scan time of qMRI. Therefore, qMRI techniques facilitated by simultaneous motion correction are of great interest.<sup>153,212</sup>

Lung imaging is only one of the least investigated application domains in the included studies. The reasons contributing to this are the lung's sparse soft tissue structures, low proton density, and larger susceptibility variations due to multiple interfaces between air and soft tissue, which

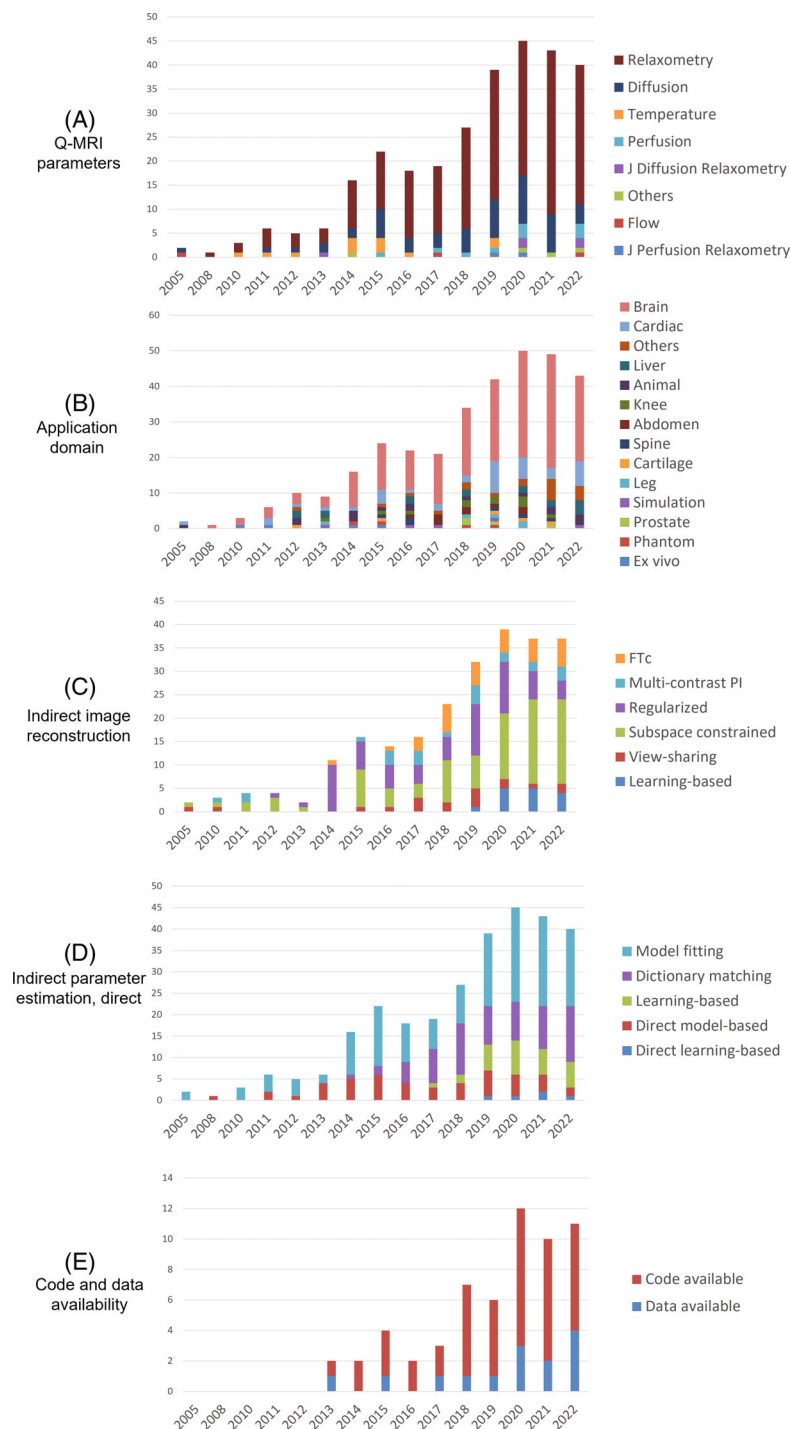


**FIGURE 7** Distribution of articles in different years: (A) the number of articles targeted on specific classes of parameters in each year, (B) the number of articles targeted on specific application domains in each year, (C) the number of articles presenting a novelty related to each subcategory of image reconstruction in each year, (D) the number of articles presenting a novelty related to each subcategory of parameter estimation and direct reconstruction in each year. (E) the number of papers that shared code and data. The year 2022 includes the articles that are published until July.

hinder MRI signal generation. The lack of multiple contrasts in lung tissue limits the clinical application of qMRI for this organ.<sup>319</sup>

Most of the techniques discussed in this work are applied to data acquired with MR sequence settings, such as echo time and flip angles, optimized for a fully sampled scan. Additionally optimizing the undersampling pattern along with MR sequence settings can further improve the results.<sup>320</sup> However, given the many possible combinations of acquisition settings and undersampling patterns,

empirical optimization of in vivo precision is impractical. Hence, efforts for in-silico evaluation, such as predicting time efficiency,<sup>12,266,320-325</sup> or accuracy,<sup>118</sup> are relevant. Recently, automated learning-based methodologies have been proposed to select an optimal sampling strategy independent of the model.<sup>326</sup> Similarly, owing to the development of modern data science tools such as auto differentiation ability, it is possible to develop neural networks to estimate parameter maps by minimizing a nonlinear loss function based on the Bloch equations.<sup>327</sup>

The present study has some limitations. Although we report on the theoretical principle behind each technique, we do not report on implementation details as this was considered beyond the scope of this work. The implementation not only affects the computational cost and run time of each technique, but the choice of solver also affects the finding of the optimal solution. We neither aim to rank techniques because comparing performance in terms of reported acceleration factor, scan time, resolution, and signal-to-noise ratio is complicated by the significant differences in anatomical locations, hardware, and parameters with which the techniques have been presented. It should be noted that recent techniques for qMRI have been proposed that directly estimate qMRI maps from a single contrast image, using data-driven strategies.<sup>328-330</sup> These techniques are not included in this study.

qMRI is a promising field, but scan time reduction is only one of the main obstacles to its clinical application. In addition to the long scan time, accurate estimation of parameters is a fundamental challenge in qMRI,<sup>331</sup> which becomes even more prominent in accelerated qMRI. The reconstruction techniques often introduce some regularization and impose assumptions on parameter values that may be invalid and bias the estimated parameters. This creates a trade-off between acceleration and accuracy, which needs to be studied prior to introducing a technique. Moreover, it is crucial to account for variabilities introduced by hardware and acquisition settings.<sup>332</sup>

To implement qMRI in clinical routines, further research on clinical interpretation of the biomarkers extracted from qMRI maps is necessary, since these biomarkers are conventionally defined on the weighted images. Synthetic weighted images produced from qMRI could bridge the direct use of quantitative maps and the current scheme where weighted images are used.<sup>133</sup> Clinical routines are often a combination of various sequences for different weighted images. A single qMRI scan from which synthetic weighted images are produced could reduce the repetitive acquisition of information shared among the weighted images, which can save scan time.

The unified mathematical framework presented in this work facilitates comparing accelerated qMRI techniques on theoretical grounds, such as the type of prior assumptions made. It highlights the essential aspects critical to the state-of-the-art qMRI reconstruction techniques, which may guide future studies. Furthermore, this review study provides an overview of the distribution of reviewed reconstruction techniques over the application domains, parameters of interest, and the years of publication, which facilitates exploring existing trends and gaps in current studies. We hope that this information helps researchers to propose new combinations of techniques or find new applications for promising techniques.

## ACKNOWLEDGMENTS

The authors wish to thank Sabrina Meertens-Gunput and Wichor Bramer from the Erasmus MC Medical Library for developing and updating the search strategies.

## ORCID

Banafshe Shafieizargar  <https://orcid.org/0000-0002-5085-4341>

Riwaj Byanju  <https://orcid.org/0000-0002-6946-7456>

Jan Sijbers  <https://orcid.org/0000-0003-4225-2487>

Stefan Klein  <https://orcid.org/0000-0003-4449-6784>

Arnold J. den Dekker  <https://orcid.org/0000-0002-0194-0198>

Dirk H. J. Poot  <https://orcid.org/0000-0003-0656-2963>

## REFERENCES

- Pierpaoli C. Quantitative brain MRI. *Top Magn Reson Imaging*. 2010;21:63.
- Seiler A, Nöth U, Hok P, et al. Multiparametric quantitative MRI in neurological diseases. *Front Neurol*. 2021;12:287.
- Ye JC. Compressed sensing MRI: a review from signal processing perspective. *BMC Biomed Eng*. 2019;1:1-17.
- Mehta BB, Coppo S, McGivney FD, et al. Magnetic resonance fingerprinting: a technical review. *Magn Reson Med*. 2019;81:25-46.
- Hsieh JJJ, Svalbe I. Magnetic resonance fingerprinting: from evolution to clinical applications. *J Med Radiat Sci*. 2020;67:333-344.
- Ding H, Velasco C, Ye H, et al. Current applications and future development of magnetic resonance fingerprinting in diagnosis, characterization, and response monitoring in cancer. *Cancer*. 2021;13(19):4742.
- Feng L, Ma D, Liu F. Rapid MR relaxometry using deep learning: an overview of current techniques and emerging trends. *NMR Biomed*. 2022;35:e4416.
- Zeng G, Guo Y, Zhan J, et al. A review on deep learning MRI reconstruction without fully sampled k-space. *BMC Med Imaging*. 2021;21:195.
- Tamir JJ, Ong F, Anand S, Karasan E, Wang K, Lustig M. Computational MRI with physics-based constraints: application to multicontrast and quantitative imaging. *IEEE Signal Process Mag*. 2020;37:94-104.
- Menon RG, Zibetti MV, Jain R, Ge Y, Regatte RR. Performance comparison of compressed sensing algorithms for accelerating T1 $\rho$  mapping of human brain. *J Magn Reson Imaging*. 2021;53:1130-1139.
- Wang X, Tan Z, Scholand N, Roeloffs V, Uecker M. Physics-based reconstruction methods for magnetic resonance imaging. *Philos Trans A Math Phys Eng Sci*. 2021;379:20200196.
- Leitão D, Teixeira RPAG, Price A, Uus A, Hajnal JV, Malik SJ. Efficiency analysis for quantitative MRI of T1 and T2 relaxometry methods. *Phys Med Biol*. 2021;66:15NT02.
- Zhu M, Zhang C, Yan J, et al. Accuracy of quantitative diffusion-weighted imaging for differentiating benign and malignant pancreatic lesions: a systematic review and meta-analysis. *EMJ Radiol*. 2021;31:7746-7759.



14. Banjar M, Horiuchi S, Gedeon DN, Yoshioka H. Review of quantitative knee articular cartilage MR imaging. *Magn Reson Med.* 2021;21:29-40.
15. Munoz C, Fotaki A, Botnar RM, Prieto C. Latest advances in image acceleration: all dimensions are fair game. *J Magn Reson Imaging.* 2023; 57: 387-402. doi:10.1002/jmri.28462
16. Page MJ, McKenzie JE, Bossuyt PM, et al. The PRISMA 2020 statement: an updated guideline for reporting systematic reviews. *Syst Rev.* 2021;10:1-11.
17. Bydder M, Larkman D, Hajnal J. Combination of signals from array coils using image-based estimation of coil sensitivity profiles. *Magn Reson Med.* 2002;47:539-548.
18. Pruessmann KP, Weiger M, Börnert P, Boesiger P. Advances in sensitivity encoding with arbitrary k-space trajectories. *Magn Reson Med.* 2001;46:638-651.
19. Griswold MA, Jakob PM, Heidemann RM, et al. Generalized autocalibrating partially parallel acquisitions (GRAPPA). *Magn Reson Med.* 2002;47:1202-1210.
20. Sijbers J, den Dekker AJ, Raman E, Van Dyck D. Parameter estimation from magnitude MR images. *Int J Imag Syst Technol.* 1999;10:109-114.
21. Karlsten OT, Verhagen R, Bovée WM. Parameter estimation from Rician-distributed data sets using a maximum likelihood estimator: application to T1 and perfusion measurements. *Magn Reson Med.* 1999;41:614-623.
22. van den Bos A. *Parameter Estimation for Scientists and Engineers.* John Wiley Sons, Inc; 2007.
23. Varadarajan D, Haldar JP. A Majorize-minimize framework for Rician and non-central chi MR images. *IEEE Trans Med Imaging.* 2015;34:2191-2202.
24. Bryant DJ, Payne JA, Firmin DN, Longmore DB. Measurement of flow with NMR imaging using a gradient pulse and phase difference technique. *J Comput Assist Tomogr.* 1984;8:588-593.
25. Bassar P, Mattiello J, Leblhan D. Estimation of the effective self-diffusion tensor from the NMR spin echo. *J Magn Reson B.* 1994;103:247-254.
26. Frahm J, Voit D, Uecker M. Real-time magnetic resonance imaging: radial gradient-echo sequences with nonlinear inverse reconstruction. *Invest Radiol.* 2019;54:757-766.
27. Shi X, Ma X, Wu W, Huang F, Yuan C, Guo H. Parallel imaging and compressed sensing combined framework for accelerating high-resolution diffusion tensor imaging using inter-image correlation. *Magn Reson Med.* 2015;73:1775-1785.
28. Bruce IP, Chang H, Petty C, Chen N, Song AW. 3D-MB-MUSE: a robust 3D multi-slab, multi-band and multi-shot reconstruction approach for ultrahigh resolution diffusion MRI. *Neuroimage.* 2017;159:46-56.
29. Mei C, Panych LP, Yuan J, et al. Combining two-dimensional spatially selective RF excitation, parallel imaging, and UNFOLD for accelerated MR thermometry imaging. *Magn Reson Med.* 2011;66:112-122.
30. Chen F, Shi X, Chen S, et al. Accelerated model-based proton resonance frequency shift temperature mapping using echo-based GRAPPA reconstruction. *Magn Reson Imaging.* 2015;33:240-245.
31. Liu W, Turkbey B, SÉNÉGAS J, et al. Accelerated T2 mapping for characterization of prostate cancer. *Magn Reson Med.* 2011;65:1400-1406.
32. Manhard MK, Bilgic B, Liao C, et al. Accelerated whole-brain perfusion imaging using a simultaneous multislice spin-echo and gradient-echo sequence with joint virtual coil reconstruction. *Magn Reson Med.* 2019;82:973-983.
33. Chen Y, Lee GR, Aandal G, et al. Rapid volumetric T1 mapping of the abdomen using three-dimensional through-time spiral GRAPPA. *Magn Reson Med.* 2016;75:1457-1465.
34. SÉNÉGAS J, Liu W, Dahnke H, Song H, Jordan EK, Frank JA. Fast T2 relaxometry with an accelerated multi-echo spin-echo sequence. *NMR Biomed.* 2010;23:958-967.
35. Wang F, Dong Z, Reese TG, et al. Echo planar time-resolved imaging (EPTI). *Magn Reson Med.* 2019;81:3599-3615.
36. Liao C, Stockmann J, Tian Q, et al. High-fidelity, high-isotropic-resolution diffusion imaging through gSlider acquisition with and T1 corrections and integrated B0/Rx shim array. *Magn Reson Med.* 2020;83:56-67.
37. Yu FF, Huang SY, Kumar A, et al. Rapid simultaneous acquisition of macromolecular tissue volume, susceptibility, and relaxometry maps. *Magn Reson Med.* 2022;87:781-790.
38. Chen Y, Fang Z, Hung S-C, Chang W-T, Shen D, Lin W. High-resolution 3D MR fingerprinting using parallel imaging and deep learning. *Neuroimage.* 2020;206:116329.
39. Ye H, Cauley SF, Gagoski B, et al. Simultaneous multislice magnetic resonance fingerprinting (SMS-MRF) with direct-spiral slice-GRAPPA (ds-SG) reconstruction. *Magn Reson Med.* 2017;77:1966-1974.
40. Ye H, Ma D, Jiang Y, et al. Accelerating magnetic resonance fingerprinting (MRF) using t-blipped simultaneous multislice (SMS) acquisition. *Magn Reson Med.* 2016;75:2078-2085.
41. Hilbert T, Schulz J, Marques JP, et al. Fast model-based T2 mapping using SAR-reduced simultaneous multislice excitation. *Magn Reson Med.* 2019;82:2090-2103.
42. Gibbons EK, Hodgson KK, Chaudhari AS, et al. Simultaneous NODDI and GFA parameter map generation from subsampled q-space imaging using deep learning. *Magn Reson Med.* 2019;81:2399-2411.
43. Ramos-Llordén G, Ning L, Liao C, et al. High-fidelity, accelerated whole-brain submillimeter in vivo diffusion MRI using gSlider-spherical ridgelets (gSlider-SR). *Magn Reson Med.* 2020;84:1781-1795.
44. Ma L, Otikovs M, Cousin SF, Liberman G, Bao Q, Frydman L. Simultaneous multi-banding and multi-echo phase encoding for the accelerated acquisition of high-resolution volumetric diffusivity maps by spatiotemporally encoded MRI. *Magn Reson Imaging.* 2021;79:130-139.
45. Gupta K, Awate SP. Random forests for simultaneous-multislice (SMS) undersampled HARDI reconstruction and uncertainty estimation. Paper presented at: 2019 IEEE International Conference on Image Processing (ICIP); 2019; Taipei, Taiwan:2626-2630.
46. Dai E, Lee PK, Dong Z, Fu F, Setsompop K, McNab JA. Distortion-free diffusion imaging using self-navigated Cartesian Echo-planar time resolved acquisition and joint magnitude and phase constrained reconstruction. *IEEE Trans Med Imaging.* 2022;41:63-74.
47. Doneva M, Börnert P, Eggers H, Stehning C, SÉNÉGAS J, Mertins A. Compressed sensing reconstruction for magnetic resonance parameter mapping. *Magn Reson Med.* 2010;64:1114-1120.
48. Beaumont J, Fripp J, Raniga P, et al. Multi T1-weighted contrast imaging and T1 mapping with Compressed sensing FLAWS at 3T. *bioRxiv.* 2021.

49. Chen HS, Majumdar A, Kozlowski P. Compressed sensing CPMG with group-sparse reconstruction for myelin water imaging. *Magn Reson Med*. 2014;71:1166-1171.
50. Wu Y, Ma X, Huang F, Guo H. Common information enhanced reconstruction for accelerated high-resolution multi-shot diffusion imaging. *Magn Reson Imaging*. 2019;62:28-37.
51. Kim D, Eisenmenger L, Turski P, Johnson KM. Simultaneous 3D-TOF angiography and 4D-flow MRI with enhanced flow signal using multiple overlapping thin slab acquisition and magnetization transfer. *Magn Reson Med*. 2022;87:1401-1417.
52. Lugauer F, Nickel D, Wetzl J, Kiefer B, Hornegger J, Maier A. Accelerating multi-echo water-fat MRI with a joint locally low-rank and spatial sparsity-promoting reconstruction. *Magma*. 2017;30:189-202.
53. Abascal JFPI, Desco M, Parra-Robles J. Incorporation of prior knowledge of signal behavior into the reconstruction to accelerate the acquisition of diffusion MRI data. *IEEE Trans Med Imaging*. 2018;37:547-556.
54. Kuei CN, Guidon A, Chang HC, Song AW. A robust multi-shot scan strategy for high-resolution diffusion weighted MRI enabled by multiplexed sensitivity-encoding (MUSE). *Neuroimage*. 2013;72:41-47.
55. Mani M, Jacob M, Magnotta V, Zhong J. Fast iterative algorithm for the reconstruction of multishot non-cartesian diffusion data. *Magn Reson Med*. 2015;74:1086-1094.
56. Mehranian A, McGinnity CJ, Neji R, et al. Motion-corrected and high-resolution anatomically assisted (MOCHA) reconstruction of arterial spin labeling MRI. *Magn Reson Med*. 2020;84:1306-1320.
57. Pandey S, Snider AD, Moreno WA, Ravi H, Bilgin A, Raghunand N. Joint total variation-based reconstruction of multiparametric magnetic resonance images for mapping tissue types. *NMR Biomed*. 2021;34:e4597.
58. Chen J, Pal P, Ahrens ET. Enhanced detection of paramagnetic fluorine-19 Magn Reson imaging agents using zero echo time sequence and compressed sensing. *NMR Biomed*. 2022;35:e4725.
59. Zi R, Zhu D, Qin Q. Quantitative T2 mapping using accelerated 3D stack-of-spiral gradient echo readout. *Magn Reson Imaging*. 2020;73:138-147.
60. Cao Z, Gore JC, Grissom WA. Low-rank plus sparse compressed sensing for accelerated proton resonance frequency shift MR temperature imaging. *Magn Reson Med*. 2019;81:3555-3566.
61. Huang J, Wang L, Chu C, Liu W, Zhu Y. Accelerating cardiac diffusion tensor imaging combining local low-rank and 3D TV constraint. *Magma (New York, NY)*. 2019;32:407-422.
62. Utzschneider M, Müller M, Gast LV, et al. Towards accelerated quantitative sodium MRI at 7 T in the skeletal muscle: comparison of anisotropic acquisition- and compressed sensing techniques. *Magn Reson Imaging*. 2021;75:72-88.
63. McClymont D, Teh I, Whittington HJ, Grau V, Schneider JE. Prospective acceleration of diffusion tensor imaging with compressed sensing using adaptive dictionaries. *Magn Reson Med*. 2016;76:248-258.
64. Tamada D, Wakayama T, Onishi H, Motosugi U. Multiparameter estimation using multi-echo spoiled gradient echo with variable flip angles and multicontrast compressed sensing. *Magn Reson Med*. 2018;80:1546-1555.
65. Roccia E, Vidya SR, Neji R, et al. Accelerated 3D T2 mapping with dictionary-based matching for prostate imaging. *Magn Reson Med*. 2019;81:1795-1805.
66. Marty B, Coppa B, Carlier P. Fast, precise, and accurate myocardial T1 mapping using a radial MOLLI sequence with FLASH readout. *Magn Reson Med*. 2018;79:1387-1398.
67. Vaish A, Gupta A, Rajwade A. MSR-Hardi: accelerated reconstruction of Haldi data using multiple sparsity regularizers. Paper presented at: 2020 IEEE International Conference on Image Processing (ICIP); 2020; Abu Dhabi, UAE:2850-2854.
68. Spann SM, Shao X, Wang DJ, et al. Robust single-shot acquisition of high resolution whole brain ASL images by combining time-dependent 2D CAPIRINHA sampling with spatio-temporal TGV reconstruction. *Neuroimage*. 2020;206:116337.
69. Burns BL, Wilson NE, Thomas MA. Group sparse reconstruction of multi-dimensional spectroscopic imaging in human brain in vivo. *Algorithms*. 2014;7:276-294.
70. Todd N, Vyas U, Bever J, Payne A, Parker DL. Reconstruction of fully three-dimensional high spatial and temporal resolution MR temperature maps for retrospective applications. *Magn Reson Med*. 2012;67:724-730.
71. Todd N, Prakash J, Odéen H, et al. Toward real-time availability of 3D temperature maps created with temporally constrained reconstruction. *Magn Reson Med*. 2014;71:1394-1404.
72. Prakash J, Todd N, Yalavarthi PK. Prior image based temporally constrained reconstruction algorithm for magnetic resonance guided high intensity focused ultrasound. *Med Phys*. 2015;42:6804-6814.
73. Odéen H, Bever J, Almquist S, et al. Treatment envelope evaluation in transcranial magnetic resonance-guided focused ultrasound utilizing 3D MR thermometry. *J Ther Ultrasound*. 2014;2:19.
74. Odéen H, Todd N, Diakite M, Minalga E, Payne A, Parker DL. Sampling strategies for subsampled segmented EPI PRF thermometry in MR guided high intensity focused ultrasound. *Med Phys*. 2014;41:092301.
75. Velikina JV, Samsonov AA. New image reconstruction methods for accelerated quantitative parameter mapping and magnetic resonance angiography. *J Phys Conf Ser*. 2016;677:012002.
76. Velikina JV, Alexander AL, Samsonov A. Accelerating MR parameter mapping using sparsity-promoting regularization in parametric dimension. *Magn Reson Med*. 2013;70:1263-1273.
77. Zong F, Du J, Deng X, et al. Fast diffusion kurtosis mapping of human brain at 7 tesla with hybrid principal component analyses. *IEEE Access*. 2021;9:107965-107975.
78. Spinner GR, Schmidt JF, Deuster C, Federau C, Stoeck CT, Kozierke S. Enhancing intravoxel incoherent motion parameter mapping in the brain using k-b PCA. *NMR Biomed*. 2018;31:e4008.
79. Peng X, Ying L, Liu X, Liang D. Accurate T2 mapping with sparsity and linear predictability filtering. Paper presented at: 2014 IEEE 11th International Symposium on Biomedical Imaging (ISBI); 2014; Beijing, China:161-164.
80. Peng X, Ying L, Liu Y, Yuan J, Liu X, Liang D. Accelerated exponential parameterization of T2 relaxation with model-driven low rank and sparsity priors (MORASA). *Magn Reson Med*. 2016;76:1865-1878.

81. Vaish A, Rajwade A, Gupta A. TL-HARDI: transform learning based accelerated reconstruction of HARDI data. *Comput Biol Med.* 2022;143:105212.
82. Huang J, Wang L, Chu C, Zhang Y, Liu W, Zhu Y. Cardiac diffusion tensor imaging based on compressed sensing using joint sparsity and low-rank approximation. *Technol Health Care.* 2016;24:S593-S599.
83. Wu Y, Zhu Y-J, Tang Q-Y, et al. Accelerated MR diffusion tensor imaging using distributed compressed sensing. *Magn Reson Med.* 2014;71:763-772.
84. Wu W, Koopmans PJ, Andersson JL, Miller KL. Diffusion acceleration with Gaussian process estimated reconstruction (DAGER). *Magn Reson Med.* 2019;82:107-125.
85. Song P, Eldar YC, Mazor G, Rodrigues MRD. HYDRA: hybrid deep magnetic resonance fingerprinting. *Med Phys.* 2019;46:4951-4969.
86. Mehta BB, Chen X, Bilchick KC, Salerno M, Epstein FH. Accelerated and navigator-gated look-locker imaging for cardiac T1 estimation (ANGIE): development and application to T1 mapping of the right ventricle. *Magn Reson Med.* 2015;73:150-160.
87. Mehta BB, Salerno M, Epstein FH. High-resolution three-dimensional ANGIE T1 mapping of the whole heart. *J Cardiovasc Magn Reson.* 2015;17:1-3.
88. Qi H, Bustin A, Cruz G, et al. Free-running simultaneous myocardial T1/T2 mapping and cine imaging with 3D whole-heart coverage and isotropic spatial resolution. *Magn Reson Imaging.* 2019;63:159-169.
89. Qi H, Jaubert O, Bustin A, et al. Free-running 3D whole heart myocardial T1 mapping with isotropic spatial resolution. *Magn Reson Med.* 2019;82:1331-1342.
90. Liao C, Chen Y, Cao X, et al. Efficient parallel reconstruction for high resolution multishot spiral diffusion data with low rank constraint. *Magn Reson Med.* 2017;77:1359-1366.
91. Mani M, Jacob M, McKinnon G, et al. SMS MUSSELS: a navigator-free reconstruction for simultaneous multi-slice-accelerated multi-shot diffusion weighted imaging. *Magn Reson Med.* 2020;83:154-169.
92. Mazor G, Weizman L, Tal A, Eldar YC. Low-rank magnetic resonance fingerprinting. *Med Phys.* 2018;45:4066-4084.
93. Hu Y, Wang X, Tian Q, et al. Multi-shot diffusion-weighted MRI reconstruction with magnitude-based spatial-angular locally low-rank regularization (SPA-LLR). *Magn Reson Med.* 2020;83:1596-1607.
94. Hu Y, Ikeda DM, Pittman SM, et al. Multishot diffusion-weighted MRI of the breast with multiplexed sensitivity encoding (MUSE) and shot locally low-rank (shot-LLR) reconstructions. *J Magn Reson Imaging.* 2021;53:807-817.
95. Zimmermann M, Abbas Z, Dzieciol K, Shah NJ. Accelerated parameter mapping of multiple-echo gradient-echo data using model-based iterative reconstruction. *IEEE Trans Med Imaging.* 2018;37:626-637.
96. Zibetti MVW, Sharafi A, Otazo R, Regatte RR. Accelerated mono- and biexponential 3D-T1 $\rho$  relaxation mapping of knee cartilage using golden angle radial acquisitions and compressed sensing. *Magn Reson Med.* 2020;83:1291-1309.
97. Tang S, Fernandez-Granda C, Lannuzel S, et al. Multicompartment magnetic resonance fingerprinting. *Inverse Probl.* 2018;34:094005.
98. Tourais J, Scannell CM, Schneider T, et al. High-resolution free-breathing quantitative first-pass perfusion cardiac MR using dual-Echo Dixon with Spatio-temporal acceleration. *Front Cardiovasc Med.* 2022;9:884221.
99. Dikaos N, Protonotarios NE, Fokas AS, Kastis GA. Quantification of T1, T2 relaxation times from magnetic resonance fingerprinting radially undersampled data using analytical transformations. *Magn Reson Imaging.* 2021;80:81-89.
100. Gao H, Li L, Zhang K, Zhou W, Hu X. PCLR: phase-constrained low-rank model for compressive diffusion-weighted MRI. *Magn Reson Med.* 2014;72:1330-1341.
101. Chen Q, She H, Du YP. Whole brain myelin water mapping in one minute using tensor dictionary learning with low-rank plus sparse regularization. *IEEE Trans Med Imaging.* 2021;40:1253-1266.
102. Bustin A, Cruz G, Jaubert O, Lopez K, Botnar RM, Prieto C. High-dimensionality undersampled patch-based reconstruction (HD-PROST) for accelerated multi-contrast MRI. *Magn Reson Med.* 2019;81:3705-3719.
103. Bustin A, Milotta G, Ismail TF, Neji R, Botnar RM, Prieto C. Accelerated free-breathing whole-heart 3D T2 mapping with high isotropic resolution. *Magn Reson Med.* 2020;83:988-1002.
104. Milotta G, Bustin A, Jaubert O, Neji R, Prieto C, Botnar RM. 3D whole-heart isotropic-resolution motion-compensated joint T1/T2 mapping and water/fat imaging. *Magn Reson Med.* 2020;84:3009-3026.
105. Milotta G, Ginami G, Bustin A, Neji R, Prieto C, Botnar RM. 3D whole-heart free-breathing qBOOST-T2 mapping. *Magn Reson Med.* 2020;83:1673-1687.
106. Saucedo A, Lefkimiatis S, Rangwala N, Sung K. Improved computational efficiency of locally low rank MRI reconstruction using iterative random patch adjustments. *IEEE Trans Med Imaging.* 2017;36:1209-1220.
107. Setsompop K, Fan Q, Stockmann J, et al. High-resolution in vivo diffusion imaging of the human brain with generalized slice dithered enhanced resolution: simultaneous multislice (gSlider-SMS). *Magn Reson Med.* 2018;79:141-151.
108. Haldar JP, Liu Y, Liao C, Fan Q, Setsompop K. Fast submillimeter diffusion MRI using gSlider-SMS and SNR-enhancing joint reconstruction. *Magn Reson Med.* 2020;84:762-776.
109. Liang Z-p. Spatiotemporal imaging with partially separable functions. Paper presented at: 2007 4th IEEE International Symposium on Biomedical Imaging: From Nano to Macro; 2007; Arlington, VA:988-991.
110. Huang C, Graff CG, Clarkson EW, Bilgin A, Altbach MI. T2 mapping from highly undersampled data by reconstruction of principal component coefficient maps using compressed sensing. *Magn Reson Med.* 2012;67:1355-1366.
111. Huang C, Bilgin A, Barr T, Altbach MI. T2 relaxometry with indirect echo compensation from highly undersampled data. *Magn Reson Med.* 2013;70:1026-1037.
112. Lima da Cruz G, Bustin A, Jaubert O, Schneider T, Botnar RM, Prieto C. Sparsity and locally low rank regularization for MR fingerprinting. *Magn Reson Med.* 2019;81:3530-3543.
113. Gutjahr FT, Kampf T, Winter P, et al. Quantification of perfusion in murine myocardium: a retrospectively triggered T1-based ASL method using model-based reconstruction. *Magn Reson Med.* 2015;74:1705-1715.
114. Hagio T, Huang C, Abidov A, et al. T2 mapping of the heart with a double-inversion radial fast spin-echo method with indirect echo compensation. *J Cardiovasc Magn Reson.* 2015;17(1):24.



115. Dong Z, Wang F, Chan KS, et al. Variable flip angle echo planar time-resolved imaging (vFA-EPTI) for fast high-resolution gradient echo myelin water imaging. *Neuroimage*. 2021;232:117897.
116. Dong Z, Wang F, Reese TG, Bilgic B, Setsompop K. Echo planar time-resolved imaging with subspace reconstruction and optimized spatiotemporal encoding. *Magn Reson Med*. 2020;84:2442-2455.
117. Feng L, Liu F, Soutanidis G, et al. Magnetization-prepared GRASP MRI for rapid 3D T1 mapping and fat/water-separated T1 mapping. *Magn Reson Med*. 2021;86:97-114.
118. Zhao B, Setsompop K, Adalsteinsson E, et al. Improved magnetic resonance fingerprinting reconstruction with low-rank and subspace modeling. *Magn Reson Med*. 2018;79:933-942.
119. Hamilton JI, Jiang Y, Eck B, Griswold M, Seiberlich N. Cardiac cine magnetic resonance fingerprinting for combined ejection fraction, T1 and T2 quantification. *NMR Biomed*. 2020;33:e4323.
120. Hamilton JI, Jiang Y, Ma D, et al. Simultaneous multislice cardiac magnetic resonance fingerprinting using low rank reconstruction. *NMR Biomed*. 2019;32:e4041.
121. Zhao B, Bilgic B, Adalsteinsson E, Griswold MA, Wald LL, Setsompop K. Simultaneous multislice magnetic resonance fingerprinting with low-rank and subspace modeling. Paper presented at: 2017 39th Annual International Conference of the IEEE Engineering in Medicine and Biology Society (EMBC); 2017; Jeju, Korea:3264-3268.
122. Keerthivasan MB, Saranathan M, Johnson K, et al. An efficient 3D stack-of-stars turbo spin echo pulse sequence for simultaneous T2-weighted imaging and T2 mapping. *Magn Reson Med*. 2019;82:326-341.
123. Lam F, Sutton BP. Intravoxel B0 inhomogeneity corrected reconstruction using a low-rank encoding operator. *Magn Reson Med*. 2020;84:885-894.
124. Li Z, Fu Z, Keerthivasan M, et al. Rapid high-resolution volumetric T1 mapping using a highly accelerated stack-of-stars look locker technique. *Magn Reson Imaging*. 2021;79:28-37.
125. Li Z, Xu X, Yang Y, Feng L. Repeatability and robustness of MP-GRASP T1 mapping. *Magn Reson Med*. 2022;87:2271-2286.
126. Wang F, Dong Z, Reese TG, Rosen B, Wald LL, Setsompop K. 3D Echo planar time-resolved imaging (3D-EPTI) for ultrafast multi-parametric quantitative MRI. *Neuroimage*. 2022;250:118963.
127. Mickevicius NJ, Kim JP, Zhao J, Morris ZS, Hurst NJ Jr, Glide-Hurst CK. Toward magnetic resonance fingerprinting for low-field MR-guided radiation therapy. *Med Phys*. 2021;48:6930-6940.
128. Mickevicius NJ, Glide-Hurst CK. Low-rank inversion reconstruction for through-plane accelerated radial MR fingerprinting applied to relaxometry at 0.35 T. *Magn Reson Med*. 2022;88:840-848.
129. Li Z, Bilgin A, Johnson K, et al. Rapid high-resolution T1 mapping using a highly accelerated radial steady-state free-precession technique. *J Magn Reson Imaging*. 2019;49:239-252.
130. Ma S, Wang N, Fan Z, et al. Three-dimensional whole-brain simultaneous T1, T2, and T1 $\rho$  quantification using MR multitasking: method and initial clinical experience in tissue characterization of multiple sclerosis. *Magn Reson Med*. 2021;85:1938-1952.
131. Golbabaee M, Chen Z, Wiaux Y, Davies M. CoverBLIP: accelerated and scalable iterative matched-filtering for magnetic resonance fingerprint reconstruction. *Inverse Probl*. 2019;36:015003.
132. Golbabaee M, Buonincontri G, Pirkel CM, et al. Compressive MRI quantification using convex spatiotemporal priors and deep encoder-decoder networks. *Med Image Anal*. 2021;69:101945.
133. Pirkel CM, Nunez-Gonzalez L, Kofler F, et al. Accelerated 3D whole-brain T1, T2, and proton density mapping: feasibility for clinical glioma MR imaging. *Neuroradiology*. 2021;63:1831-1851.
134. Pirkel CM, Cencini M, Kurzwaski JW, et al. Learning residual motion correction for fast and robust 3D multiparametric MRI. *Med Image Anal*. 2022;77:102387.
135. Roeloffs V, Uecker M, Frahm J. Joint T1 and T2 mapping with tiny dictionaries and subspace-constrained reconstruction. *IEEE Trans Med Imaging*. 2020;39:1008-1014.
136. Dong Z, Wang F, Wald L, Setsompop K. SNR-efficient distortion-free diffusion relaxometry imaging using accelerated echo-train shifted echo-planar time-resolving imaging (ACE-EPTI). *Magn Reson Med*. 2022;88:164-179.
137. Jaubert O, Cruz G, Bustin A, et al. Free-running cardiac magnetic resonance fingerprinting: joint T1/T2 map and cine imaging. *Magn Reson Imaging*. 2020;68:173-182.
138. Jaubert O, Cruz G, Bustin A, et al. Water-fat Dixon cardiac magnetic resonance fingerprinting. *Magn Reson Med*. 2020;83:2107-2123.
139. Velasco C, Cruz G, Lavin B, et al. Simultaneous T1, T2, and T1 $\rho$  cardiac magnetic resonance fingerprinting for contrast agent-free myocardial tissue characterization. *Magn Reson Med*. 2022;87:1992-2002.
140. Mandava S, Keerthivasan MB, Li Z, Martin DR, Altbach MI, Bilgin A. Accelerated MR parameter mapping with a union of local subspaces constraint. *Magn Reson Med*. 2018;80:2744-2758.
141. Cruz G, Qi H, Jaubert O, et al. Generalized low-rank nonrigid motion-corrected reconstruction for MR fingerprinting. *Magn Reson Med*. 2022;87:746-763.
142. Cruz GJ, Velasco C, Lavin B, Jaubert O, Botnar RM, Prieto C. Myocardial T1, T2, T2\*, and fat fraction quantification via low-rank motion-corrected cardiac MR fingerprinting. *Magn Reson Med*. 2022;87:2757-2774.
143. Berman BP, Keerthivasan MB, Li Z, Martin DR, Altbach MI, Bilgin A. Dictionary learning for compressive parameter mapping in Magn Reson imaging. In: Manos P, Goyal VK, van De VD, eds. *Proc Wavelets and Sparsity XVI*. International Society for Optics and Photonics; 2015: 34-42.
144. Assländer J, Cloos MA, Knoll F, Sodickson DK, Hennig J, Lattanzi R. Low rank alternating direction method of multipliers reconstruction for MR fingerprinting. *Magn Reson Med*. 2018;79:83-96.
145. Cao T, Ma S, Wang N, et al. Three-dimensional simultaneous brain mapping of T1, T2, and magnetic susceptibility with MR multitasking. *Magn Reson Med*. 2022;87:1375-1389.
146. Zhang C, Arefin TM, Nakarmi U, et al. Acceleration of three-dimensional diffusion magnetic resonance imaging using a kernel low-rank compressed sensing method. *Neuroimage*. 2020;210:116584.



147. Zhou Y, Wang H, Liu Y, Liang D, Ying L. Accelerating MR parameter mapping using nonlinear compressive manifold learning and regularized pre-imaging. *IEEE Trans Biomed Eng*. 2022;69:2996-3007.
148. Zhou Y, Shi C, Ren F, Lyu J, Liang D, Ying L. Accelerating MR parameter mapping using nonlinear manifold learning and supervised pre-imaging. Paper presented at: 2015 IEEE 12th International Symposium on Biomedical Imaging (ISBI); 2015; Brooklyn, NY:897-900.
149. Bhavé S, Lingala SG, Johnson CP, Magnotta VA, Jacob M. Accelerated whole-brain multi-parameter mapping using blind compressed sensing. *Magn Reson Med*. 2016;75:1175-1186.
150. Kargas N, Weingärtner S, Sidiropoulos ND, Akçakaya M. Low-rank tensor regularization for improved dynamic quantitative magnetic resonance imaging. Paper presented at: *Proceedings of Signal Processing with Adaptive Sparse Structured Representations Workshop (SPARS)*; 2017; Lisbon, Portugal.
151. Han PK, Horng DE, Marin T, et al. Free-breathing three-dimensional T1 mapping of the heart using subspace-based data acquisition and image reconstruction. Paper presented at: 2019 41st Annual International Conference of the IEEE Engineering in Medicine and Biology Society (EMBC); 2019; Berlin, Germany:4008-4011.
152. Cao T, Wang N, Kwan AC, et al. Free-breathing, non-ECG, simultaneous myocardial T1, T2, T2\*, and fat-fraction mapping with motion-resolved cardiovascular MR multitasking. *Magn Reson Med*. 2022;88:1748-1763.
153. Ma S, Wang N, Xie Y, Fan Z, Li D, Christodoulou AG. Motion-robust quantitative multiparametric brain MRI with motion-resolved MR multitasking. *Magn Reson Med*. 2022;87:102-119.
154. Zhao B, Setsompop K, Salat D, Wald LL. Further development of subspace imaging to magnetic resonance fingerprinting: a low-rank tensor approach. Paper presented at: 2020 42nd Annual International Conference of the IEEE Engineering in Medicine & Biology Society (EMBC); 2020; Montreal, Canada:1662-1666.
155. Wang N, Christodoulou AG, Xie Y, et al. Quantitative 3D dynamic contrast-enhanced (DCE) MR imaging of carotid vessel wall by fast T1 mapping using multitasking. *Magn Reson Med*. 2019;81:2302-2314.
156. Yaman B, Weingärtner S, Kargas N, Sidiropoulos ND, Akçakaya M. Low-rank tensor models for improved multidimensional MRI: application to dynamic cardiac T1 mapping. *IEEE Trans Comput Imaging*. 2020;6:194-207.
157. Yu Y, Jin J, Liu F, Crozier S. Multidimensional compressed sensing MRI using tensor decomposition-based sparsifying transform. *PLoS One*. 2014;9:1-13.
158. Christodoulou AG, Shaw JL, Nguyen C, et al. Magnetic resonance multitasking for motion-resolved quantitative cardiovascular imaging. *Nat Biomed Eng*. 2018;2:215-226.
159. Ma S, Nguyen CT, Han F, et al. Three-dimensional simultaneous brain T1, T2, and ADC mapping with MR multitasking. *Magn Reson Med*. 2020;84:72-88.
160. Mao X, Lee HL, Hu Z, et al. Simultaneous multi-slice cardiac MR multitasking for motion-resolved, non-ECG, free-breathing T1-T2 mapping. *Front Cardiovasc Med*. 2022;9:833257.
161. Wang N, Cao T, Han F, et al. Free-breathing multitasking multi-echo MRI for whole-liver water-specific T1, proton density fat fraction, and quantification. *Magn Reson Med*. 2022;87:120-137.
162. Cheng J, Shen D, Basser PJ, Yap PT. Joint 6D k-q space compressed sensing for accelerated high angular resolution diffusion MRI. Paper presented at: International Conference on Information Processing in Medical Imaging 2015; Isle of Skye, UK; 2015:782-793.
163. Ma S, Nguyen CT, Christodoulou AG, et al. Accelerated cardiac diffusion tensor imaging using joint low-rank and sparsity constraints. *IEEE Trans Biomed Eng*. 2018;65:2219-2230.
164. Zhao B, Lu W, Hitchens TK, Lam F, Ho C, Liang Z-P. Accelerated MR parameter mapping with low-rank and sparsity constraints. *Magn Reson Med*. 2015;74:489-498.
165. Han PK, Marin T, Djebra Y, et al. Free-breathing 3D cardiac T1 mapping with transmit B1 correction at 3T. *Magn Reson Med*. 2022;87:1832-1845.
166. Mandava S, Keerthivasan MB, Martin DR, Altbach MI, Bilgin A. Improving subspace constrained radial fast spin echo MRI using block matching driven non-local low rank regularization. *Phys Med Biol*. 2021;66:04NT03.
167. Cao X, Liao C, Iyer SS, et al. Optimized multi-axis spiral projection MR fingerprinting with subspace reconstruction for rapid whole-brain high-isotropic-resolution quantitative imaging. *Magn Reson Med*. 2022;88:133-150.
168. Keerthivasan MB, Galons J-P, Johnson K, et al. Abdominal T2-weighted imaging and T2 mapping using a variable flip angle radial turbo spin-echo technique. *J Magn Reson Imaging*. 2022;55:289-300.
169. West DJ, Cruz G, Teixeira RPAG, et al. An MR fingerprinting approach for quantitative inhomogeneous magnetization transfer imaging. *Magn Reson Med*. 2022;87:220-235.
170. Zhang X, Duchemin Q, Liu\* K, et al. Cramér-Rao bound-informed training of neural networks for quantitative MRI. *Magn Reson Med*. 2022;88:436-448.
171. Lee D, Kim EY, Yoon H, Park S, Ye JC. T2 prime mapping from highly undersampled data using compressed sensing with patch based low rank penalty. Paper presented at: 2014 IEEE 11th International Symposium on Biomedical Imaging (ISBI); Beijing, China; 2014:645-648.
172. Wen Q, Feng L, Zhou K, Wu Y. Rapid golden-angle diffusion-weighted propeller MRI for simultaneous assessment of ADC and IVIM. *Neuroimage*. 2020;223:117327.
173. Meng Z, Guo R, Li Y, et al. Accelerating T2 mapping of the brain by integrating deep learning priors with low-rank and sparse modeling. *Magn Reson Med*. 2021;85:1455-1467.
174. Milshteyn E, Morze C, Reed GD, et al. Using a local low rank plus sparse reconstruction to accelerate dynamic hyperpolarized 13C imaging using the bSSFP sequence. *J Magn Reson*. 2018;290:46-59.
175. Zhu YJ, Liu YY, Ying L, et al. SCOPE: signal compensation for low-rank plus sparse matrix decomposition for fast parameter mapping. *Phys Med Biol*. 2018;63(18):185009.
176. Zhu Y, Liu Y, Ying L, Liu X, Zheng H, Liang D. Bio-SCOPE: fast biexponential T1ρ mapping of the brain using signal-compensated low-rank plus sparse matrix decomposition. *Magn Reson Med*. 2020;83:2092-2106.
177. Liu Y, Ying L, Chen W, et al. Accelerating the 3D T1ρ mapping of cartilage using a signal-compensated robust tensor principal component analysis model. *Quant Imaging Med Surg*. 2021;11(8):3376-3391.

178. Li Y, Wang Y, Qi H, et al. Deep learning-enhanced T1 mapping with spatial-temporal and physical constraint. *Magn Reson Med*. 2021;86:1647-1661.
179. Mani M, Jacob M, Kelley D, Magnotta V. Multi-shot sensitivity-encoded diffusion data recovery using structured low-rank matrix completion (MUSSELS). *Magn Reson Med*. 2017;78:494-507.
180. Mani M, Aggarwal HK, Magnotta V, Jacob M. Improved MUSSELS reconstruction for high-resolution multi-shot diffusion weighted imaging. *Magn Reson Med*. 2020;83:2253-2263.
181. Bilgic B, Chatnuntawech I, Manhard MK, et al. Highly accelerated multishot echo planar imaging through synergistic machine learning and joint reconstruction. *Magn Reson Med*. 2019;82:1343-1358.
182. Lee D, Jin KH, Kim EY, Park S-H, Ye JC. Acceleration of MR parameter mapping using annihilating filter-based low rank hankel matrix (ALOHA). *Magn Reson Med*. 2016;76:1848-1864.
183. Hu Y, Li P, Chen H, Zou L, Wang H. High-quality MR fingerprinting reconstruction using structured low-rank matrix completion and subspace projection. *IEEE Trans Med Imaging*. 2022;41:1150-1164.
184. Cao X, Wang K, Liao C, et al. Efficient T2 mapping with blip-up/down EPI and gSlider-SMS (T2-BUDA-gSlider). *Magn Reson Med*. 2021;86:2064-2075.
185. Liao C, Bilgic B, Tian Q, et al. Distortion-free, high-isotropic-resolution diffusion MRI with gSlider BUDA-EPI and multicoil dynamic B0 shimming. *Magn Reson Med*. 2021;86:791-803.
186. Zhang Z, Cho J, Wang L, et al. Blip up-down acquisition for spin- and gradient-echo imaging (BUDA-SAGE) with self-supervised denoising enables efficient T2, T2\*, Para- and dia-magnetic susceptibility mapping. *Magn Reson Med*. 2022;88:633-650.
187. Li P, Hu Y. MR fingerprinting reconstruction using structured low-rank matrix recovery and subspace modeling. Paper presented at: 2021 IEEE 18th International Symposium on Biomedical Imaging (ISBI); 2021; Nice, France:1214-1217.
188. Aggarwal HK, Mani MP, Jacob M. MoDL-MUSSELS: model-based deep learning for multishot sensitivity-encoded diffusion MRI. *IEEE Trans Med Imaging*. 2020;39:1268-1277.
189. Li W, Griswold M, Yu X. Fast cardiac T1 mapping in mice using a model-based compressed sensing method. *Magn Reson Med*. 2012;68:1127-1134.
190. Utzschneider M, Behl NGR, Lachner S, et al. T-2\* accelerated quantification of tissue sodium concentration in skeletal muscle tissue: quantitative capability of dictionary learning compressed sensing. *Magn Reson Mater Phys Biol Med*. 2020;33:495-505.
191. Zhou R, Weller DS, Yang Y, et al. Dual-excitation flip-angle simultaneous cine and T1 mapping using spiral acquisition with respiratory and cardiac self-gating. *Magn Reson Med*. 2021;86:82-96.
192. Liu D, Steingotter A, Parker HL, Curcic J, Kozerke S. Accelerating MRI fat quantification using a signal model-based dictionary to assess gastric fat volume and distribution of fat fraction. *Magn Reson Imaging*. 2017;37:81-89.
193. Zhu Y, Kang J, Duan C, et al. Integrated motion correction and dictionary learning for free-breathing myocardial T1 mapping. *Magn Reson Med*. 2019;81:2644-2654.
194. Zhu Y, Zhang Q, Liu Q, et al. PANDA-T1p: integrating principal component analysis and dictionary learning for fast T1p mapping. *Magn Reson Med*. 2015;73:263-272.
195. Jiang Y, Hsu EW. Accelerating MR diffusion tensor imaging via filtered reduced-encoding projection-reconstruction. *Magn Reson Med*. 2005;53:93-102.
196. Cruz G, Schneider T, Bruijnen T, Gaspar AS, Botnar RM, Prieto C. Accelerated magnetic resonance fingerprinting using soft-weighted key-hole (MRF-SOHO). *PLoS One*. 2018;13:1-18.
197. Buonincontri G, Sawiak SJ. MR fingerprinting with simultaneous B1 estimation. *Magn Reson Med*. 2016;76:1127-1135.
198. Todd N, Payne A, Parker DL. Model predictive filtering for improved temporal resolution in MRI temperature imaging. *Magn Reson Med*. 2010;63:1269-1279.
199. Darçot E, Yerly J, Colotti R, et al. Accelerated and high-resolution cardiac T2 mapping through peripheral k-space sharing. *Magn Reson Med*. 2019;81:220-233.
200. Svedin BT, Dillon CR, Parker DL. Effect of k-space-weighted image contrast and ultrasound focus size on the accuracy of proton resonance frequency thermometry. *Magn Reson Med*. 2019;81:247-257.
201. Fan L, Hong K, Hsu L-Y, et al. Optimal saturation recovery time for minimizing the underestimation of arterial input function in quantitative cardiac perfusion MRI. *Magn Reson Med*. 2022;88:832-839.
202. Lugand E, Yerly J, Feliciano H, Chaptinel J, Stuber M, Van Heeswijk RB. Accelerated and KWIC-filtered cardiac T2 mapping for improved precision: proof of principle. *J Cardiovasc Magn Reson*. 2015;17(Suppl 1):W30.
203. Alexandra Cristobal Huerta MWVGPK, Hernandez-Tamames JA. K-space trajectories in 3D-GRASE sequence for high resolution structural imaging. *Magn Reson Imaging*. 2018;48:10-19.
204. Chan RW, Lau AZ, Detzler G, Thayalasuthan V, Nam RK, Haider MA. Evaluating the accuracy of multicomponent T2 parameters for luminal water imaging of the prostate with acceleration using inner-volume 3D GRASE. *Magn Reson Med*. 2019;81:466-476.
205. Cao X, Liao C, Wang Z, et al. Robust sliding-window reconstruction for accelerating the acquisition of MR fingerprinting. *Magn Reson Med*. 2017;78:1579-1588.
206. Wen Q, Kodiweera C, Dale BM, Shivraman G, Wu Y-C. Rotating single-shot acquisition (RoSA) with composite reconstruction for fast high-resolution diffusion imaging. *Magn Reson Med*. 2018;79:264-275.
207. Nagtegaal M, Koken P, Amthor T, et al. Myelin water imaging from multi-echo T2 MR relaxometry data using a joint sparsity constraint. *Neuroimage*. 2020;219:117014.
208. Liao C, Bilgic B, Manhard MK, et al. 3D MR fingerprinting with accelerated stack-of-spirals and hybrid sliding-window and GRAPPA reconstruction. *Neuroimage*. 2017;162:13-22.
209. Pirk CM, Gómez PA, Lipp I, et al. Deep learning-based parameter mapping for joint relaxation and diffusion tensor MR fingerprinting. *Proceedings of Medical Imaging with Deep Learning*. PMLR; 2020:638-654.
210. Piredda GF, Hilbert T, Canales-Rodríguez EJ, et al. Fast and high-resolution myelin water imaging: accelerating multi-echo GRASE with CAIPIRINHA. *Magn Reson Med*. 2021;85:209-222.
211. Cao P, Wang Z, Liu C, Li T, Hui ES, Cai J. Motion-resolved and free-breathing liver MRF. *Magn Reson Imaging*. 2022;91:69-80.
212. Hu Y, Xu Y, Tian Q, et al. RUN-UP: accelerated multishot diffusion-weighted MRI reconstruction using an unrolled network with U-net as priors. *Magn Reson Med*. 2021;85:709-720.

213. Mani MP, Aggarwal HK, Ghosh S, Jacob M. Model-based deep learning for reconstruction of joint k-q under-sampled high resolution diffusion MRI. Paper presented at: 2020 IEEE 17th International Symposium on Biomedical Imaging (ISBI); 2020; Iowa City, IA:913-916.
214. Zibetti MVW, Johnson PM, Sharafi A, Hammernik K, Knoll F, Regatte RR. Rapid mono and biexponential 3D-T<sub>1</sub> $\rho$  mapping of knee cartilage using variational networks. *Sci Rep.* 2020;10:19144.
215. Gong K, Han P, El Fakhri G, Ma C, Li Q. Arterial spin labeling MR image denoising and reconstruction using unsupervised deep learning. *NMR Biomed.* 2022;35(4):e4224.
216. Mani M, Yang B, Bathla G, Magnotta V, Jacob M. Multi-band and in-plane-accelerated diffusion MRI enabled by model-based deep learning in q-space and its extension to learning in the spherical harmonic domain. *Magn Reson Med.* 2022;87:1799-1815.
217. Mani M, Magnotta VA, Jacob M. qModel: a plug-and-play model-based reconstruction for highly accelerated multi-shot diffusion MRI using learned priors. *Magn Reson Med.* 2021;86:835-851.
218. Fatania K, Pirkel C, Menzel M, Hall P, Golbabaee M. A plug-and-play approach to multiparametric quantitative MRI: image reconstruction using pre-trained deep denoisers. Paper presented at: Proceedings of IEEE International Symposium on Biomedical Imaging, ISBI; April 17, 2022.
219. Gao Y, Cloos M, Liu F, Crozier S, Pike GB, Sun H. Accelerating quantitative susceptibility and R2\* mapping using incoherent undersampling and deep neural network reconstruction. *Neuroimage.* 2021;240:118404.
220. Ji S, Jeong J, Oh S-H, et al. Quad-contrast imaging: simultaneous acquisition of four contrast-weighted images (PD-weighted, T2-weighted, PD-FLAIR and T2-FLAIR images) with synthetic T1-weighted image, T1- and T2-maps. *IEEE Trans Med Imaging.* 2021;40:3617-3626.
221. Duan C, Deng H, Xiao S, et al. Accelerate gas diffusion-weighted MRI for lung morphometry with deep learning. *Eur Radiol.* 2022;32:702-713.
222. Fu Z, Mandava S, Keerthivasan MB, et al. A multi-scale residual network for accelerated radial MR parameter mapping. *Magn Reson Imaging.* 2020;73:152-162.
223. Wu Y, Ma Y, Du J, Xing L. Accelerating quantitative MR imaging with the incorporation of B1 compensation using deep learning. *Magn Reson Imaging.* 2020;72:78-86.
224. Shih S-F, Kafali SG, Armstrong T, Zhong X, Calkins KL, Wu HH. Deep learning-based parameter mapping with uncertainty estimation for fat quantification using accelerated free-breathing radial MRI. Paper presented at: Proceedings of IEEE International Symposium on Biomedical Imaging (ISBI); 2021; Nice, France:433-437.
225. Yang J, Zhang ZC, Zhu YC, Xie YQ. An accurate estimation of T2\* mapping for fast magnetic resonance imaging. *Proceedings of International Symposium on Image Computing and Digital Medicine.* Association for Computing Machinery; 2019:335-342.
226. Lattanzi R, Zhang B, Knoll F, Assländer J, Cloos MA. Phase unwinding for dictionary compression with multiple channel transmission in magnetic resonance fingerprinting. *Magn Reson Imaging.* 2018;49:32-38.
227. Deshmane A, McGivney DF, Ma D, et al. Partial volume mapping using magnetic resonance fingerprinting. *NMR Biomed.* 2019;32:e4082.
228. Körzdörfer G, Jiang Y, Speier P, et al. Magnetic resonance field fingerprinting. *Magn Reson Med.* 2018;81:2347-2359.
229. Ma D, Jiang Y, Chen Y, et al. Fast 3D magnetic resonance fingerprinting for a whole-brain coverage. *Magn Reson Med.* 2018;79:2190-2197.
230. van Valenberg W, Klein S, Vos FM, Koolstra K, Vliet LJ, Poot DHJ. An efficient method for multi-parameter mapping in quantitative MRI using B-spline interpolation. *IEEE Trans Med Imaging.* 2020;39:1681-1689.
231. Yang M, Ma D, Jiang Y, et al. Low rank approximation methods for MR fingerprinting with large scale dictionaries. *Magn Reson Med.* 2018;79:2392-2400.
232. Jiang Y, Ma D, Bhat H, et al. Use of pattern recognition for unaliasing simultaneously acquired slices in simultaneous multi-slice MR fingerprinting. *Magn Reson Med.* 2017;78:1870-1876.
233. Wang Z, Li H, Zhang Q, Yuan J, Wang X. Magnetic resonance fingerprinting with compressed sensing and distance metric learning. *Neurocomputing.* 2016;174:560-570.
234. MacAskill CJ, Markley M, Farr S, et al. Rapid B1-insensitive MR fingerprinting for quantitative kidney imaging. *Radiology.* 2021;300:380-387.
235. Pierre EY, Ma D, Chen Y, Badve C, Griswold MA. Multi-scale reconstruction for MR fingerprinting. *Magn Reson Med.* 2016;75:2481-2492.
236. Ma D, Gulani V, Seiberlich N, et al. Magnetic resonance fingerprinting. *Nature.* 2013;495:187-192.
237. Amthor T, Doneva M, Koken P, Sommer K, Meineke J, Börner P. Magnetic resonance fingerprinting with short relaxation intervals. *Magn Reson Imaging.* 2017;41:22-28.
238. Ben-Eliezer N, Sodickson DK, Block KT. Rapid and accurate T2 mapping from multi-spin-echo data using Bloch-simulation-based reconstruction. *Magn Reson Med.* 2015;73:809-817.
239. Marriott A, Bowen C, Rioux J, Brewer K. Simultaneous quantification of SPIO and gadolinium contrast agents using MR fingerprinting. *Magn Reson Imaging.* 2021;79:121-129.
240. Nagtegaal M, Koken P, Amthor T, Doneva M. Fast multi-component analysis using a joint sparsity constraint for MR fingerprinting. *Magn Reson Med.* 2020;83:521-534.
241. Rieger B, Zimmer F, Zapp J, Weingärtner S, Schad LR. Magnetic resonance fingerprinting using echo-planar imaging: joint quantification of T1 and relaxation times. *Magn Reson Med.* 2017;78:1724-1733.
242. Gu Y, Wang L, Yang H, et al. Three-dimensional high-resolution T1 and T2 mapping of whole macaque brain at 9.4 T using magnetic resonance fingerprinting. *Magn Reson Med.* 2022;87:2901-2913.
243. Körzdörfer G, Pfeuffer J, Kluge T, et al. Effect of spiral under-sampling patterns on FISP MRF parameter maps. *Magn Reson Imaging.* 2019;62:174-180.
244. Boyacioglu R, Wang C, Ma D, McGivney DF, Yu X, Griswold MA. 3D magnetic resonance fingerprinting with quadratic RF phase. *Magn Reson Med.* 2021;85:2084-2094.
245. Shpringer G, Bendahan D, Ben-Eliezer N. Accelerated reconstruction of dictionary-based T2 relaxation maps based on dictionary compression and gradient descent search algorithms. *Magn Reson Imaging.* 2022;87:56-66.



246. Marty B, Lopez Kolkovsky AL, Araujo EC, Reyngoudt H. Quantitative skeletal muscle imaging using 3D MR fingerprinting with water and fat separation. *J Magn Reson Imaging*. 2021;53:1529-1538.
247. Fang Z, Chen Y, Lin W, Shen D. Quantification of relaxation times in MR fingerprinting using deep learning. *Proceedings of International Society of Magnetic Resonance in Medicine*; 2017:25.
248. Fang Z, Chen Y, Liu M, et al. Deep learning for fast and spatially constrained tissue quantification from highly accelerated data in magnetic resonance fingerprinting. *IEEE Trans Med Imaging*. 2019;38:2364-2374.
249. Fang Z, Chen Y, Hung S-C, Zhang X, Lin W, Shen D. Sub-millimeter MR fingerprinting using deep learning-based tissue quantification. *Magn Reson Med*. 2020;84:579-591.
250. Zhang Q, Su P, Chen Z, et al. Deep learning-based MR fingerprinting ASL ReconStruction (DeepMARS). *Magn Reson Med*. 2020;84:1024-1034.
251. Hermann I, Martínez-Heras E, Rieger B, et al. Accelerated white matter lesion analysis based on simultaneous T1 and T2 quantification using magnetic resonance fingerprinting and deep learning. *Magn Reson Med*. 2021;86:471-486.
252. Cohen O, Zhu B, Rosen MS. MR fingerprinting deep RecOnstruction NEtwork (DRONE). *Magn Reson Med*. 2018;80:885-894.
253. Hamilton JI, Currey D, Rajagopalan S, Seiberlich N. Deep learning reconstruction for cardiac magnetic resonance fingerprinting T1 and T2 mapping. *Magn Reson Med*. 2021;85:2127-2135.
254. Hoppe E, Thamm F, Korzdorfer G, et al. RinQ fingerprinting: recurrence-informed quantile networks for magnetic resonance fingerprinting. *Proceedings of Medical Image Computing and Computer Assisted Intervention*. Lecture Notes in Computer Science. Vol 11766. Springer International Publishing Ag; 2019:92-100.
255. Ulas C, Tetteh G, Thrippleton MJ, et al. Direct estimation of pharmacokinetic parameters from DCE-MRI using deep CNN with forward physical model loss. *Proceedings of Medical Image Computing and Computer Assisted Intervention*. Lecture Notes in Computer Science. Vol 11070. Springer International Publishing Ag; 2018:39-47.
256. Hong J-S, Hermann I, Zöllner FG, et al. Acceleration of magnetic resonance fingerprinting reconstruction using denoising and self-attention pyramidal convolutional neural network. *Sensors*. 2022;22(3):1260.
257. Khajehim M, Christen T, Tam F, Graham SJ. Streamlined magnetic resonance fingerprinting: fast whole-brain coverage with deep-learning based parameter estimation. *Neuroimage*. 2021;238:118237.
258. Li S, Wu J, Ma L, Cai S, Cai C. A simultaneous multi-slice T2 mapping framework based on overlapping-echo detachment planar imaging and deep learning reconstruction. *Magn Reson Med*. 2022;87:2239-2253.
259. Ouyang B, Yang Q, Wang X, et al. Single-shot T2 mapping via multi-echo-train multiple overlapping-echo detachment planar imaging and multitask deep learning. *Med Phys*. 2022;49(11):7095-7107. doi:10.1002/mp.15820
260. Cao P, Cui D, Vardhanabhuti V, Hui ES. Development of fast deep learning quantification for magnetic resonance fingerprinting in vivo. *Magn Reson Imaging*. 2020;70:81-90.
261. Zhang J, Wu J, Chen S, et al. Robust single-shot T2 mapping via multiple overlapping-echo acquisition and deep neural network. *IEEE Trans Med Imaging*. 2019;38:1801-1811.
262. Nataraj G, Nielsen J-F, Scott C, Fessler JA. Dictionary-free MRI PERK: parameter estimation via regression with kernels. *IEEE Trans Med Imaging*. 2018;37:2103-2114.
263. Barbieri M, Brizi L, Giampieri E, et al. A deep learning approach for magnetic resonance fingerprinting: scaling capabilities and good training practices investigated by simulations. *Phys Med*. 2021;89:80-92.
264. Soyak R, Navruz E, Ersoy EO, et al. Channel attention networks for robust MR fingerprint matching. *IEEE Trans Biomed Eng*. 2022;69:1398-1405.
265. Sumpf TJ, Uecker M, Boretius S, Frahm J. Model-based non-linear inverse reconstruction for T2 mapping using highly undersampled spin-echo MRI. *J Magn Reson Imaging*. 2011;34:420-428.
266. Welsh CL, Hsu EW, Di Bella EV. Strategies for undersampling and reconstructing MR DTI data. Paper presented at: 2011 IEEE International Symposium on Biomedical Imaging: From Nano to Macro; Chicago, Illinois, USA; 2011:77-80.
267. Ben-Eliezer N, Sodickson DK, Shepherd T, Wiggins GC, Block KT. Accelerated and motion-robust in vivo T2 mapping from radially undersampled data using bloch-simulation-based iterative reconstruction. *Magn Reson Med*. 2016;75:1346-1354.
268. Pesce M, Repetti A, Wiaux Y. Fast spatially coherent fiber orientation estimation in diffusion MRI from kq-space sampling. Paper presented at: 2019 IEEE 8th International Workshop on Computational Advances in Multi-Sensor Adaptive Processing (CAMSAP); 2019; Le gosier, Guadeloupe:326-330.
269. Welsh CL, Dibella EV, Adluru G, Hsu EW. Model-based reconstruction of undersampled diffusion tensor k-space data. *Magn Reson Med*. 2013;70:429-440.
270. Tran-Gia J, Wech T, Bley T, Köstler H. Model-based acceleration of look-locker T1 mapping. *PLoS One* 2015;10:1-15.
271. Zhu Z, Lebel RM, Bliesener Y, Acharya J, Frayne R, Nayak KS. Sparse precontrast T1 mapping for high-resolution whole-brain DCE-MRI. *Magn Reson Med*. 2021;86:2234-2249.
272. Wiens CN, McCurdy CM, Willig-Onwuachi JD, McKenzie CA. R2\*-corrected water-fat imaging using compressed sensing and parallel imaging. *Magn Reson Med*. 2014;71:608-616.
273. Zhao L, Feng X, Meyer CH. Direct and accelerated parameter mapping using the unscented Kalman filter. *Magn Reson Med*. 2016;75:1989-1999.
274. Sumpf TJ, Petrovic A, Uecker M, Knoll F, Frahm J. Fast T2 mapping with improved accuracy using undersampled spin-Echo MRI and model-based reconstructions with a generating function. *IEEE Trans Med Imaging*. 2014;33:2213-2222.
275. Dong G, Hintermüller M, Papafitsoros K. Quantitative Magn Reson imaging: from fingerprinting to integrated physics-based models. *SIAM J Imag Sci*. 2019;12:927-971.
276. Zhao B. Model-based iterative reconstruction for magnetic resonance fingerprinting. Paper presented at: 2015 IEEE International Conference on Image Processing (ICIP); 2015; Quebec City, Canada:3392-3396.
277. Zhao B, Setsompop K, Ye H, Cauley SF, Wald LL. Maximum likelihood reconstruction for magnetic resonance fingerprinting. *IEEE Trans Med Imaging*. 2016;35:1812-1823.



278. van der Heide O, Sbrizzi A, Berg CAT. Accelerated MR-STAT reconstructions using sparse hessian approximations. *IEEE Trans Med Imaging*. 2020;39:3737-3748.
279. Hu C, Reeves SJ. Trust region methods for the estimation of a complex exponential decay model in MRI with a single-shot or multi-shot trajectory. *IEEE Trans Image Process*. 2015;24:3694-3706.
280. Schneider M, Benkert T, Solomon E, et al. Free-breathing fat and R2\* quantification in the liver using a stack-of-stars multi-echo acquisition with respiratory-resolved model-based reconstruction. *Magn Reson Med*. 2020;84:2592-2605.
281. Sharma SD, Hu HH, Nayak KS. Accelerated T2\*-compensated fat fraction quantification using a joint parallel imaging and compressed sensing framework. *J Magn Reson Imaging*. 2013;38:1267-1275.
282. Lankford CL, Dortch RD, Does MD. Fast T2 mapping with multiple echo, caesar cipher acquisition and model-based reconstruction. *Magn Reson Med*. 2015;73:1065-1074.
283. Wang X, Roeloffs V, Klosowski J, et al. Model-based T1 mapping with sparsity constraints using single-shot inversion-recovery radial FLASH. *Magn Reson Med*. 2018;79:730-740.
284. Wang X, Kohler F, Unterberg-Buchwald C, Lotz J, Frahm J, Uecker M. Model-based myocardial T1 mapping with sparsity constraints using single-shot inversion-recovery radial FLASH cardiovascular magnetic resonance. *J Cardiovasc Magn Reson*. 2018;79(2):730-740.
285. Wang X, Rosenzweig S, Scholand N, Holme HCM, Uecker M. Model-based reconstruction for simultaneous multi-slice mapping using single-shot inversion-recovery radial FLASH. *Magn Reson Med*. 2021;85:1258-1271.
286. Dikaos N. Stochastic gradient Langevin dynamics for joint parameterization of tracer kinetic models, input functions, and T1 relaxation-times from undersampled k-space DCE-MRI. *Med Image Anal*. 2020;62:101690.
287. Shafieizargar B, Jeurissen B, Poot DHJ, den Dekker AJ, Sijbers J. Multi-contrast multi-shot EPI for accelerated diffusion MRI. Paper presented at: 2021 43rd Annual International Conference of the IEEE Engineering in Medicine & Biology Society (EMBC); 2021; Mexico:3869-3872.
288. Shafieizargar B, Jeurissen B, Poot DHJ, et al. ADEPT: accurate diffusion echo-planar imaging with multi-contrast shotS. *Magn Reson Med*. 2023;89:396-410.
289. Gaur P, Grissom WA. Accelerated MRI thermometry by direct estimation of temperature from undersampled k-space data. *Magn Reson Med*. 2015;73:1914-1925.
290. Pesce M, Repetti A, Auria A, Daducci A, Thiran J-P, Wiaux Y. Fast Fiber orientation estimation in diffusion MRI from kq-space sampling and anatomical priors. *J Imag*. 2021;7(11):226.
291. Knoll F, Raya JG, Halloran RO, et al. A model-based reconstruction for undersampled radial spin-echo DTI with variational penalties on the diffusion tensor. *NMR Biomed*. 2015;28:353-366.
292. Dong Z, Dai E, Wang F, et al. Model-based reconstruction for simultaneous multislice and parallel imaging accelerated multishot diffusion tensor imaging. *Med Phys*. 2018;45:3196-3204.
293. Hüfken T, Arbogast JM, Bracher A-K, Beer M, Neubauer H, Rasche V. Accelerated model-based quantitative diffusion MRI: a feasibility study for musculoskeletal application. *Z Med Phys*. 2022;32:240-247.
294. Hanhela M, Pajanen A, Nissi MJ, Kolehmainen V. Embedded quantitative MRI T1ρ; mapping using non-linear primal-dual proximal splitting. *J Imag*. 2022;8(6):157.
295. Peng X, Liu X, Zheng H, Liang D. Exploiting parameter sparsity in model-based reconstruction to accelerate proton density and T2 mapping. *Med Eng Phys*. 2014;36:1428-1435.
296. Wang X, Voit D, Roeloffs V, Uecker M, Frahm J. Fast interleaved multislice T1 mapping: model-based reconstruction of single-shot inversion-recovery radial FLASH. *Comp Math Methods Med*. 2018;2560964.
297. Zhao B, Lam F, Liang Z-P. Model-based MR parameter mapping with sparsity constraints: parameter estimation and performance bounds. *IEEE Trans Med Imaging*. 2014;33:1832-1844.
298. Guo Y, Lingala SG, Zhu Y, Lebel RM, Nayak KS. Direct estimation of tracer-kinetic parameter maps from highly undersampled brain dynamic contrast enhanced MRI. *Magn Reson Med*. 2017;78:1566-1578.
299. Maier O, Schoormans J, Schloegl M, et al. Rapid T1 quantification from high resolution 3D data with model-based reconstruction. *Magn Reson Med*. 2019;81:2072-2089.
300. Sun J, Sakhaee E, Entezari A, Vemuri BC. Leveraging EAP-sparsity for compressed sensing of MS-HARDI in (k, q)-space. *Inf Process Med Imaging*. 2015;24:375-386.
301. Sun J, Entezari A, Vemuri BC. Exploiting structural redundancy in q-space for improved EAP reconstruction from highly undersampled (k, q)-space in DMRI. *Med Image Anal*. 2019;54:122-137.
302. Olafsson VT, Noll DC, Fessler JA. Fast joint reconstruction of dynamic R2\* and field maps in functional MRI. *IEEE Trans Med Imaging*. 2008;27:1177-1188.
303. Zhu Y, Wu Y, Zheng Y, Wu EX, Ying L, Liang D. A model-based method with joint sparsity constraint for direct diffusion tensor estimation. Paper presented at: 2012 9th IEEE International Symposium on Biomedical Imaging (ISBI); 2012; Barcelona, Spain:510-513.
304. Eliasi PA, Feng L, Otazo R, Rangan S. Fast magnetic resonance parametric imaging via structured low-rank matrix reconstruction. Paper presented at: 2014 48th Asilomar Conference on Signals, Systems and Computers; 2014; Pacific Grove, CA:423-428.
305. Awate SP, Di Bella EVR. Compressed sensing HARDI via rotation-invariant concise dictionaries, flexible K-space undersampling, and multiscale spatial regularity. Paper presented at: 2013 IEEE 10th International Symposium on Biomedical Imaging; 2013; San Francisco, CA:9-12.
306. Hilbert T, Sumpf TJ, Weiland E, et al. Accelerated T2 mapping combining parallel MRI and model-based reconstruction: GRAPPATINI. *J Magn Reson Imaging*. 2018;48:359-368.
307. Raudner M, Schreiner M, Hilbert T, et al. Accelerated T2 mapping of the lumbar intervertebral disc: highly undersampled k-space data for robust T2 relaxation time measurement in clinically feasible acquisition times. *Invest Radiol*. 2020;55:695-701.
308. Raudner M, Schreiner MM, Hilbert T, et al. Clinical implementation of accelerated T2 mapping: quantitative Magn Reson imaging as a biomarker for annular tear and lumbar disc herniation. *Eur Radiol*. 2020;31(6):3590-3599.
309. Sbrizzi A, Heide O, Cloos M, et al. Fast quantitative MRI as a nonlinear tomography problem. *Magn Reson Imaging*. 2018;46:56-63.

310. Hu C, Peters DC. SUPER: a blockwise curve-fitting method for accelerating MR parametric mapping with fast reconstruction. *Magn Reson Med*. 2019;81:3515-3529.
311. Tan Z, Hohage T, Kalentev O, et al. An eigenvalue approach for the automatic scaling of unknowns in model-based reconstructions: application to real-time phase-contrast flow MRI. *NMR Biomed*. 2017;30:e3835.
312. Liu F, Feng L, Kijowski R. MANTIS: model-augmented neural network with incoherent k-space sampling for efficient MR parameter mapping. *Magn Reson Med*. 2019;82:174-188.
313. Liu F, Kijowski R, El Fakhri G, Feng L. Magnetic resonance parameter mapping using model-guided self-supervised deep learning. *Magn Reson Med*. 2021;85:3211-3226.
314. Jun Y, Shin H, Eo T, Kim T, Hwang D. Deep model-based magnetic resonance parameter mapping network (DOPAMINE) for fast T1 mapping using variable flip angle method. *Med Image Anal*. 2021;70:102017.
315. Liu H, Heide O, Mandija S, Berg CAT, Sbrizzi A. Acceleration strategies for MR-STAT: achieving high-resolution reconstructions on a desktop PC within 3 minutes. *IEEE Trans Med Imaging*. 2022;41(10):2681-2692.
316. Liu Y, Chen Y, Yap P-T. Real-time mapping of tissue properties for magnetic resonance fingerprinting. In: Marleen B, Cattin Philippe C, Stéphane C, et al., eds. *Medical Image Computing and Computer Assisted Intervention – MICCAI 2021*. Springer, Cham. 2021;12906:161-170.
317. Wu W, Miller KL. Image formation in diffusion MRI: a review of recent technical developments. *J Magn Reson Imaging*. 2017;46:646.
318. Kamphuis ME, Greuter MJW, Slart RHJA, Slump CH. Quantitative imaging: systematic review of perfusion/flow phantoms. *EMJ Radiol Exp*. 2020;4:15.
319. Wielpütz M, Kauczor HU. MRI of the lung: state of the art. *Diagn Interv Radiol*. 2012;18:344-353.
320. Stolk CC, Sbrizzi A. Understanding the combined effect of k-space Undersampling and transient states excitation in MR fingerprinting reconstructions. *IEEE Trans Med Imaging*. 2019;38:2445-2455.
321. Byanju R, Klein S, Cristobal-Huerta A, Hernandez-Tamames JA, Poot DHJ. Time efficiency analysis for undersampled quantitative MRI acquisitions. *Med Image Anal*. 2022;78:102390.
322. Filipiak P, Fick R, Petiet A, et al. Reducing the number of samples in spatiotemporal dMRI acquisition design. *Magn Reson Med*. 2019;81:3218-3233.
323. Madankan R, Stefan W, Fahrenholtz SJ, et al. Accelerated magnetic resonance thermometry in the presence of uncertainties. *Phys Med Biol*. 2017;62:214-245.
324. Seo S, Luu HM, Choi SH, Park S-H. Simultaneously optimizing sampling pattern for joint acceleration of multi-contrast MRI using model-based deep learning. *Med Phys*. 2022;49:5964-5980.
325. Zibetti MVW, Herman GT, Regatte RR. Fast data-driven learning of parallel MRI sampling patterns for large scale problems. *Sci Rep*. 2021;11:19312.
326. Blumberg SB, Lin H, Grussu F, Zhou Y, Figini M, Alexander DC. Progressive subsampling for oversampled data - application to quantitative MRI. *Med Image Comput Comput Assist Interv*. 2022;13436:421-431.
327. Kang B, Kim B, Schär M, Park H, Heo H-Y. Unsupervised learning for magnetization transfer contrast MR fingerprinting: application to CEST and nuclear Overhauser enhancement imaging. *Magn Reson Med*. 2021;85:2040-2054.
328. Moya-Sáez E, Peña-Nogales O, Luis-García R, Alberola-López C. A deep learning approach for synthetic MRI based on two routine sequences and training with synthetic data. *Comput Methods Programs Biomed*. 2021;210:106371.
329. Wu Y, Ma Y, Kovalchuk N, Du J, Xing L. Retrospective tuning of MRI contrast from a single T1-weighted image. *Int J Radiat Oncol Biol Phys*. 2021;111:100.
330. Wu Y, Ma Y, Du J, Xing L. Deciphering tissue relaxation parameters from a single MR image using deep learning. Paper presented at: Proceedings of SPIE 11314, Medical Imaging 2020: Computer-Aided Diagnosis. SPIE; Houston, Texas, USA. 2020.
331. Veraart J, Poot DHJ, Van Hecke W, et al. More accurate estimation of diffusion tensor parameters using diffusion kurtosis imaging. *Magn Reson Med*. 2011;65:138-145.
332. Karakuzu A, Biswas L, Cohen-Adad J, Stikov N. Vendor-neutral sequences and fully transparent workflows improve inter-vendor reproducibility of quantitative MRI. *Magn Reson Med*. 2022;88:1212-1228.
333. Balsiger F, Jungo A, Scheidegger O, Carlier PG, Reyes M, Marty B. Spatially regularized parametric map reconstruction for fast magnetic resonance fingerprinting. *Med Image Anal*. 2020;64:101741.
334. Wang F, Dong Z, Chen S, et al. Fast temperature estimation from undersampled k-space with fully-sampled center for MR guided microwave ablation. *Magn Reson Imaging*. 2016;34:1171-1180.
335. Zhang T, Pauly JM, Levesque IR. Accelerating parameter mapping with a locally low rank constraint. *Magn Reson Med*. 2015;73:655-661.
336. Feng L, Otazo R, Jung H, et al. Accelerated cardiac T2 mapping using breath-hold multiecho fast spin-echo pulse sequence with k-t FOCUSS. *Magn Reson Med*. 2011;65:1661-1669.
337. Baltes C, Kozerke S, Hansen MS, Pruessmann KP, Tsao J, Boesiger P. Accelerating cine phase-contrast flow measurements using k-t BLAST and k-t SENSE. *Magn Reson Med*. 2005;54:1430-1438.
338. Mani M, Jacob M, Guidon A, Magnotta V, Zhong J. Acceleration of high angular and spatial resolution diffusion imaging using compressed sensing with multichannel spiral data. *Magn Reson Med*. 2015;73:126-138.
339. Petzschner FH, Ponce IP, Blaimer M, Jakob PM, Breuer FA. Fast MR parameter mapping using k-t principal component analysis. *Magn Reson Med*. 2011;66:706-716.
340. Zhou Y, Pandit P, Pedoia V, et al. Accelerating T1 $\rho$  cartilage imaging using compressed sensing with iterative locally adapted support detection and JSENSE. *Magn Reson Med*. 2016;75:1617-1629.
341. Roeloffs V, Wang X, Sumpf TJ, Untenberger M, Voit D, Frahm J. Model-based reconstruction for T1 mapping using single-shot inversion-recovery radial FLASH. *Int J Imag Syst Technol*. 2016;26:254-263.

**How to cite this article:** Shafieizargar B, Byanju R, Sijbers J, Klein S, den Dekker AJ, Poot DHJ. Systematic review of reconstruction techniques for accelerated quantitative MRI. *Magn Reson Med*. 2023;90:1172-1208. doi: 10.1002/mrm.29721

## APPENDIX

TABLE A1 List of the symbols and mathematical notations.

Symbol	Description
$(\square)$	Functional dependency
$ \square $	Number of elements
$\ \square\ _l$	Denotes $l$ th norm
$\tilde{\square}$	Defines continuous space or parameters
$\hat{\square}$	Estimated parameter
$\{\square\}$	Concatenation
<b>bold letters</b>	Vectors
$n_{\square}$	Number of elements in dimension $\square$
$\mathbf{C} \in \mathbb{C}^{n^i \times n^j}$	Coil sensitivity maps
$\mathbf{D} \in \mathbb{C}^{n^c \times n^d}$	Dictionary of signal evolutions
$d^q$	Index for digitization step for each parameter in the dictionary
$\mathcal{E} \in \mathbb{C}^{n^s n^k n^i \times n^c n^j}$	Encoding operator that maps images to k-space
$\mathcal{H}$	Neural network
$\mathbf{I} \in \mathbb{C}^{n^c \times n^j}$	Matrix of contrast images
$\mathcal{L}$	Loss function
$\mathbb{L} \in \mathbb{C}^{n^c \times n^j}$	The low-rank component of $\mathbf{I}$ when $\mathbf{I}$ is separated into its sparse and low-rank component
$\mathcal{M}$	Function that computes the difference between the simulated signal and the reconstructed signal
$m$	Index for motion states
$\mathbf{N} \in \mathbb{C}^{n^c \times n^s \times n^k}$	Array of complex valued, zero-mean Gaussian noise
$n^b$	Number of basis functions selected in low-rank reconstruction (indexed by $b$ )
$n^c$	Number of contrasts (indexed by $c$ )
$n^d$	Product of the digitization steps for each parameter in the dictionary, indexed by $d$ ( $n^d = \prod_q n^{d_q}$ )
$n^i$	Number of sparsifying transforms in a regularized reconstruction (indexed by $i$ )
$n^j$	Number of voxels in each contrast image (indexed by $j$ )
$n^k$	Number of k-space samples per contrast state (indexed by $k$ )
$n^q$	Number of qMRI parameters estimated in a scan (indexed by $q$ )
$n^s$	Number of coil sensitivity maps (indexed by $s$ )
$n^t$	Number of training datasets in deep learning approaches (indexed by $t$ )
$\mathcal{P}_j$	Patch selection operator
$\mathbf{r}_j \in \mathbb{R}^3$	3D image space coordinate
$\mathcal{S}$	Operator that converts the Fourier representation of images into defined structured matrices
$\mathbb{S} \in \mathbb{C}^{n^c \times n^j}$	The sparse component of $\mathbf{I}$ when $\mathbf{I}$ is separated into its sparse and low-rank component
$\mathcal{U} : \mathbb{R}^{n^q \times n^j} \rightarrow \mathbb{R}^{n^c \times n^j}$	Function representing a signal model
$\mathbf{v} \in \mathbb{R}^3$	3D Fourier space coordinate
$\mathbf{W}$	Output of a neural network
$\mathbf{W}_t$	Training dataset for a neural network (reference)
$\mathbf{X} \in \mathbb{R}^{n^j \times n^q}$	Matrix of parameters
$\mathbf{Y} \in \mathbb{C}^{n^c \times n^s \times n^k}$	Array of acquired k-space points

TABLE A1 (Continued)

Symbol	Description
$\tilde{Z}$	Input of a neural network
$Z_t$	Training dataset for a neural network (undersampled)
$\Gamma \in \mathbb{C}^{n^c \times n^{b_2}}$	Motion basis function
$\gamma$	Low-rank regularizer weight
$\theta$	Trainable parameters of a neural network
$\lambda$	Sparsity-based regularizer weight
$\sigma \in \mathbb{C}^{n^b \times n^j}$	Spatial weight
$\tilde{\sigma} \in \mathbb{C}^{n^{b_1} \times n^{b_2} \times n^j}$	Tensor representing spatial weights for two basis functions with $n^{b_1}$ and $n^{b_2}$ basis functions selected
$\phi$	Sparsifying operator
$\psi \in \mathbb{C}^{n^c \times n^b}$	Subspace basis function matrix with $n^b$ basis functions
$\tilde{\psi} \in \mathbb{C}^{n^c \times n^{b_1}}$	Subspace basis function matrix with $n^{b_1}$ basis functions
$\Omega \subset \mathbb{R}^3$	3D Fourier space

TABLE A2 The search query used for each database.

Database	Query
Embase.com	('imaging'/exp OR 'nuclear magnetic resonance imaging'/exp OR (fingerprint* OR MRF OR MR OR magnetic-resonan* OR qMRI OR CPMG-sequence* OR MRI OR imaging):ab,ti,kw) AND ('acceleration'/de OR 'deep learning'/de OR (under-sampl* OR undersampl* OR accelerat* OR low-rank* OR compress*-sens* OR constrain* OR sub-space* OR subspace* OR deep-learning*):ab,ti,kw) AND ('diffusion tensor imaging'/de OR 'diffusion weighted imaging'/de OR 'magnetic resonance thermometry'/exp OR (diffus*-weight* OR T1 OR T2 OR T2STAR OR T-1 OR T-2 OR T-2STAR OR relaxometr* OR myelin-water* -fract* OR diffusion*-kurtos* OR (diffusion* NEAR/3 (imag* OR MRI OR MR)) OR R1 OR R2 OR R2STAR OR DTI OR DWI OR DKI OR (quantit* NEAR/3 (magn*-reson* OR MRI OR MR)) OR ((MR OR magnetic-resonan*) NEAR/3 (thermo* OR temperature*)) OR IVIM OR intravoxel-incoherent-motion*):ab,ti,kw) AND ('image reconstruction'/de OR (reconstruct* OR mapping* OR estimat*):ab,ti,kw)
Medline	(exp Magnetic Resonance Imaging/ OR (fingerprint* OR MRF OR MR OR magnetic-resonan* OR qMRI OR CPMG-sequence* OR MRI OR imaging).ab,ti,kf.) AND (Acceleration/ OR Deep Learning/ OR (under-sampl* OR undersampl* OR accelerat* OR low-rank* OR compress*-sens* OR constrain* OR sub-space* OR subspace* OR deep-learning*). ab,ti,kf.) AND (Multiparametric Magnetic Resonance Imaging/ OR exp Diffusion Magnetic Resonance Imaging/ OR (diffus*-weight* OR T1 OR T2 OR T2STAR OR T-1 OR T-2 OR T-2STAR OR relaxometr* OR myelin-water*-fract* OR diffusion*-kurtos* OR (diffusion* ADJ3 (imag* OR MRI OR MR)) OR R1 OR R2 OR R2STAR OR DTI OR DWI OR DKI OR (quantit* ADJ3 (magn*-reson* OR MRI OR MR)) OR ((MR OR magnetic-resonan*) ADJ3 (thermo* OR temperature*)) OR IVIM OR intravoxel-incoherent-motion*).ab,ti,kf.) AND (Image Processing, Computer-Assisted/ OR (reconstruct* OR mapping* OR estimat*).ab,ti,kf.)
Cochrane Central	((fingerprint* OR MRF OR MR OR magnetic NEXT resonan* OR qMRI OR CPMG NEXT sequence* OR MRI OR imaging):ab,ti,kw) AND ((under NEXT sampl* OR undersampl* OR accelerat* OR low NEXT rank* OR compress* NEXT sens* OR constrain* OR sub NEXT space* OR subspace* OR deep NEXT learning*):ab,ti,kw) AND ((diffus* NEXT weight* OR T1 OR T2 OR T2STAR OR T NEXT 1 OR T NEXT 2 OR T NEXT 2STAR OR relaxometr* OR myelin NEXT water* NEXT fract* OR diffusion* NEXT kurtos* OR (diffusion* NEAR/3 (imag* OR MRI OR MR)) OR R1 OR R2 OR R2STAR OR DTI OR DWI OR DKI OR (quantit* NEAR/3 (magn* NEXT reson* OR MRI OR MR)) OR ((MR OR magnetic NEXT resonan*) NEAR/3 (thermo* OR temperature*)) OR IVIM OR intravoxel NEXT incoherent NEXT motion*):ab,ti,kw) AND ((reconstruct* OR mapping* OR estimat*):ab,ti,kw)



TABLE A2 (Continued)

Database	Query
Web of Science	(TI=(fingerprint* OR MRF OR MR OR magnetic-resonan* OR qMRI OR CPMG-sequence* OR MRI OR imaging) OR AB=(fingerprint* OR MRF OR MR OR magnetic-resonan* OR qMRI OR CPMG-sequence* OR MRI OR imaging)) AND (TI=(under-sampl* OR undersampl* OR accelerat* OR low-rank* OR compress*-sens* OR constrain* OR sub-space* OR subspace* OR deep-learning*) OR AB=(under-sampl* OR undersampl* OR accelerat* OR low-rank* OR compress*-sens* OR constrain* OR sub-space* OR subspace* OR deep-learning*)) AND (TI=(diffus*-weight* OR T1 OR T2 OR T2STAR OR T-1 OR T-2 OR T-2STAR OR relaxometr* OR myelin-water*-fract* OR diffusion*-kurtos* OR (diffusion* NEAR/2 (imag* OR MRI OR MR)) OR R1 OR R2 OR R2STAR OR DTI OR DWI OR DKI OR (quanti* NEAR/2 (magn*-reson* OR MRI OR MR)) OR ((MR OR magnetic-resonan*) NEAR/2 (thermo* OR temperature*)) OR IVIM OR intravoxel-incoherent-motion*) OR AB=(diffus*-weight* OR T1 OR T2 OR T2STAR OR T-1 OR T-2 OR T-2STAR OR relaxometr* OR myelin-water*-fract* OR diffusion*-kurtos* OR (diffusion* NEAR/2 (imag* OR MRI OR MR)) OR R1 OR R2 OR R2STAR OR DTI OR DWI OR DKI OR (quanti* NEAR/2 (magn*-reson* OR MRI OR MR)) OR ((MR OR magnetic-resonan*) NEAR/2 (thermo* OR temperature*)) OR IVIM OR intravoxel-incoherent-motion*)) AND (TI=(reconstruct* OR mapping* OR estimat*) OR AB=(reconstruct* OR mapping* OR estimat*))
Google Scholar	"under-sampling" undersampling acceleration model-based low-rank "low rank" "deep learning" "q  quantitative MRI" "diffusion imaging  MRI weighted" T1 T2 R1 R2 DTI DWI DKI reconstructed reconstruction mapping map mapped  estimation estimated

**TABLE A3** List of the reviewed papers labeled with first authors' last names (Author) along with the year of the publication (year), reference number in this paper (Ref), focused qMRI parameter (Parameter), qMRI reconstruction categories that are proposed considering indirect and direct techniques (category) and the subcategories used for image reconstruction (Recon) and parameter estimation (Param) in indirect categories, application domain with respect to the type of the study (App) and the organ that is studied (Organ), and finally the accessibility of the study regarding the links to data or code that are provided (Data/Code).

Author	Year	References	Parameter	Category	Recon	Param	App	Organ	Data/code
Ben-Eliezer	2014	<a href="#">238</a>	Rel	Indirect	FTc	DM	Human	Brain	<a href="#">L1</a>
Boyacioglu	2021	<a href="#">244</a>	Rel	Indirect	FTc	DM	Human	Brain	NA
Amthor	2017	<a href="#">237</a>	Rel	Indirect	FTc	DM	Human	Brain	NA
Deshmane	2018	<a href="#">227</a>	Rel	Indirect	FTc	DM	Human	Brain	NA
Jiang	2017	<a href="#">232</a>	Rel	Indirect	FTc	DM	Human	Brain	NA
Korzdorfer	2018	<a href="#">228</a>	Rel	Indirect	FTc	DM	Human	Brain, Abdomen	NA
Korzdorfer	2019	<a href="#">243</a>	Rel	Indirect	FTc	DM	Human	Brain	NA
Lattanzi	2018	<a href="#">226</a>	Rel	Indirect	FTc	DM	Human	Leg	<a href="#">L1</a>
Ma	2018	<a href="#">229</a>	Rel	Indirect	FTc	DM	Human	Brain	NA
Pierre	2016	<a href="#">235</a>	Rel	Indirect	FTc	DM	Human	Brain	NA
Valenberg	2019	<a href="#">230</a>	Rel	Indirect	FTc	DM	Human	Brain	<a href="#">L1</a>
Yang	2018	<a href="#">231</a>	Rel	Indirect	FTc	DM	Human	Brain	NA
Gu	2022	<a href="#">242</a>	Rel	Indirect	FTc	DM	Human	Brain	NA
MacAskill	2021	<a href="#">234</a>	Rel	Indirect	FTc	DM	Human	Kidney	NA
Marriott	2021	<a href="#">239</a>	Rel	Indirect	FTc	DM	In vitro	In vitro	NA
Marty	2020	<a href="#">246</a>	Rel	Indirect	FTc	DM	Human	Leg, MSK	<a href="#">L1</a>
Shpringer	2022	<a href="#">245</a>	Rel	Indirect	FTc	DM	Human	Brain, Calf	NA

TABLE A3 (Continued)

Author	Year	References	Parameter	Category	Recon	Param	App	Organ	Data/code
Nagtegaal	2020	<a href="#">240</a>	Rel	Indirect	FTc	DM	Human	Brain	<a href="#">L1</a>
Balsiger	2020	<a href="#">333</a>	Rel	Indirect	FTc	LB	Human	Leg	<a href="#">L1</a>
Fang	2020	<a href="#">249</a>	Rel	Indirect	FTc	LB	Human	Brain	NA
Fang	2017	<a href="#">247</a>	Rel	Indirect	FTc	LB	Human	Brain	<a href="#">L1</a>
Fang	2019	<a href="#">248</a>	Rel	Indirect	FTc	LB	Human	Brain	NA
Hamilton	2021	<a href="#">253</a>	Rel	Indirect	FTc	LB	Human	Cardiac	NA
Hermann	2021	<a href="#">251</a>	Rel	Indirect	FTc	LB	Human	Brain	NA
Cao	2020	<a href="#">260</a>	Rel	Indirect	FTc	LB	Human	Brain	NA
Hoppe	2019	<a href="#">254</a>	Rel	Indirect	FTc	LB	Human	Brain	NA
Ulas	2018	<a href="#">255</a>	Per	Indirect	FTc	LB	Human	Brain	NA
Zhang	2019	<a href="#">261</a>	Rel	Indirect	FTc	LB	Human	Brain	NA
Barbieri	2022	<a href="#">263</a>	Rel	Indirect	FTc	LB	Simulation	Simulation	NA
Li	2022	<a href="#">258</a>	Rel	Indirect	FTc	LB	Rat	Brain	NA
Ouyang	2022	<a href="#">259</a>	Rel	Indirect	FTc	LB	Human	Brain	NA
Soyak	2022	<a href="#">264</a>	Rel	Indirect	FTc	LB	Human	Brain	NA
Chen	2016	<a href="#">33</a>	Rel	Indirect	PI	MF	Human	Abdomen	NA
Bruce	2017	<a href="#">28</a>	Diff	Indirect	PI	MF	Human	Brain	NA
Chen	2015	<a href="#">30</a>	Temp	Indirect	PI	MF	Human	Breast	NA
Liu	2011	<a href="#">31</a>	Rel	Indirect	PI	MF	Human	Cardiac	NA
Manhard	2019	<a href="#">32</a>	PR	Indirect	PI	MF	Human	Brain	NA
Mei	2011	<a href="#">29</a>	Temp	Indirect	PI	MF	Ex vivo	Muscle	NA
Senegas	2010	<a href="#">34</a>	Rel	Indirect	PI	MF	Human	Brain	NA
Wang	2016	<a href="#">334</a>	Temp	Indirect	PI	MF	Human	Liver, Spine	NA
Wang	2019	<a href="#">35</a>	Rel	Indirect	PI	MF	Human	Brain	NA
Dai	2022	<a href="#">46</a>	DR	Indirect	PI	MF	Human	Brain	NA
Ma	2021	<a href="#">44</a>	Diff	Indirect	PI	MF	Human	Brain	NA
Yu	2022	<a href="#">37</a>	Rel	Indirect	PI	MF	Human	Brain	NA
Rieger	2017	<a href="#">241</a>	Rel	Indirect	PI	DM	Human	Brain	NA
Ye	2017	<a href="#">39</a>	Rel	Indirect	PI	DM	Human	Brain	NA
Ye	2016	<a href="#">40</a>	Rel	Indirect	PI	DM	Human	Brain	NA
Chen	2020	<a href="#">38</a>	Rel	Indirect	PI	LB	Human	Brain	NA
Cohen	2018	<a href="#">252</a>	Rel	Indirect	PI	LB	Human	Brain	NA
Gibbons	2019	<a href="#">42</a>	Diff	Indirect	PI	LB	Human	Brain	NA
Gupta	2019	<a href="#">45</a>	Diff	Indirect	PI	LB	Human	Brain	NA
Zhang	2020	<a href="#">250</a>	Per	Indirect	PI	LB	Human	Brain	NA
Hong	2022	<a href="#">256</a>	Rel	Indirect	PI	LB	Human	Brain	NA
Khajehim	2021	<a href="#">257</a>	Rel	Indirect	PI	LB	Human	Brain	<a href="#">L1</a>
Abascal	2018	<a href="#">53</a>	Diff	Indirect	RR	MF	Human	Lung	<a href="#">L1</a>
Chen	2014	<a href="#">49</a>	Rel	Indirect	RR	MF	Rat	Spine	NA

TABLE A3 (Continued)

Author	Year	References	Parameter	Category	Recon	Param	App	Organ	Data/code
Chen	2016	<a href="#">54</a>	Diff	Indirect	RR	MF	Human	Brain	NA
Cao	2019	<a href="#">60</a>	Temp	Indirect	RR	MF	Human	Leg	NA
Frahm	2019	<a href="#">26</a>	Rel	Indirect	RR	MF	Human	Brain	NA
Gao	2014	<a href="#">100</a>	Diff	Indirect	RR	MF	Human	Brain	NA
Haldar	2020	<a href="#">108</a>	Diff	Indirect	RR	MF	Human	Brain	NA
Hu	2021	<a href="#">94</a>	Diff	Indirect	RR	MF	Human	Breast	<a href="#">L1</a>
Hu	2020	<a href="#">93</a>	Diff	Indirect	RR	MF	Human	Brain	<a href="#">L1</a>
Huang	2016	<a href="#">82</a>	Diff	Indirect	RR	MF	Human	Cardiac	NA
Huang	2019	<a href="#">61</a>	Diff	Indirect	RR	MF	Human	Cardiac	<a href="#">L1</a>
Lee	2014	<a href="#">171</a>	Rel	Indirect	RR	MF	Human	Brain	NA
Liao	2017	<a href="#">90</a>	Diff	Indirect	RR	MF	Human	Brain	NA
Lugauer	2017	<a href="#">52</a>	Rel	Indirect	RR	MF	Human	Abdomen	NA
Mani	2015	<a href="#">55</a>	Diff	Indirect	RR	MF	Human	Brain	NA
Mani	2019	<a href="#">91</a>	Diff	Indirect	RR	MF	Human	Brain	NA
Mehranian	2020	<a href="#">56</a>	Per	Indirect	RR	MF	Human	Brain	<a href="#">L1</a>
Mehta	2015	<a href="#">86</a>	Rel	Indirect	RR	MF	Human	Cardiac	NA
Mehta	2015	<a href="#">87</a>	Rel	Indirect	RR	MF	Human	Cardiac	NA
Odeen	2014	<a href="#">73</a>	Temp	Indirect	RR	MF	Lamb	Brain	NA
Odeen	2014	<a href="#">74</a>	Temp	Indirect	RR	MF	Phantom	Phantom	NA
Peng	2014	<a href="#">79</a>	Rel	Indirect	RR	MF	Human	Brain	NA
Peng	2016	<a href="#">80</a>	Rel	Indirect	RR	MF	Human	Brain, Knee	NA
Prakash	2015	<a href="#">72</a>	Temp	Indirect	RR	MF	Ex vivo	Ex vivo	NA
Ramos Llorden	2020	<a href="#">43</a>	Diff	Indirect	RR	MF	Human	Brain	NA
Saucedo	2017	<a href="#">106</a>	Rel	Indirect	RR	MF	Human	Brain, Abdomen	NA
Shi	2015	<a href="#">27</a>	Diff	Indirect	RR	MF	Human	Brain	NA
Spann	2020	<a href="#">68</a>	Per	Indirect	RR	MF	Human	Brain	NA
Spinner	2018	<a href="#">78</a>	Diff	Indirect	RR	MF	Human	Brain	NA
Tamada	2018	<a href="#">64</a>	Rel	Indirect	RR	MF	Human	Liver	NA
Todd	2014	<a href="#">71</a>	Temp	Indirect	RR	MF	Ex vivo	Ex vivo	NA
Todd	2012	<a href="#">70</a>	Temp	Indirect	RR	MF	Human	Brain, Muscle	NA
Velikina	2013	<a href="#">76</a>	Rel	Indirect	RR	MF	Human	Brain	NA
Velikina	2016	<a href="#">75</a>	Rel	Indirect	RR	MF	Human	Brain	NA
Wu	2019	<a href="#">84</a>	Diff	Indirect	RR	MF	Human	Brain	NA
Wu	2019	<a href="#">50</a>	Diff	Indirect	RR	MF	Human	Brain	NA
Wu	2014	<a href="#">83</a>	Diff	Indirect	RR	MF	Rat	Cardiac	NA
Zhang	2014	<a href="#">335</a>	Rel	Indirect	RR	MF	Human	Brain	NA
Zi	2020	<a href="#">59</a>	Rel	Indirect	RR	MF	Human	Brain	NA
Zibetti	2019	<a href="#">96</a>	Rel	Indirect	RR	MF	Human	Knee	NA

TABLE A3 (Continued)

Author	Year	References	Parameter	Category	Recon	Param	App	Organ	Data/code
Zimmermann	2017	<a href="#">95</a>	Rel	Indirect	RR	MF	Human	Brain	NA
Beaumont	2021	<a href="#">48</a>	Rel	Indirect	RR	MF	Human	Brain	<a href="#">L1</a>
Burns	2014	<a href="#">69</a>	Spec	Indirect	RR	MF	Human	Brain	NA
Chen	2022	<a href="#">58</a>	F-19	Indirect	RR	MF	Mouse	Dendritic cell	NA
Kim	2022	<a href="#">51</a>	Flow	Indirect	RR	MF	Human	Brain	NA
Pandey	2021	<a href="#">57</a>	Rel	Indirect	RR	MF	Mouse	Body	NA
Tourais	2022	<a href="#">98</a>	Per	Indirect	RR	MF	Human	Cardiac	NA
Vaish	2020	<a href="#">67</a>	Diff	Indirect	RR	MF	Human	Brain	NA
Vaish	2022	<a href="#">81</a>	Diff	Indirect	RR	MF	Human	Brain	NA
Zong	2021	<a href="#">77</a>	Diff	Indirect	RR	MF	Human	Brain	NA
Bustin	2019	<a href="#">102</a>	Rel	Indirect	RR	DM	Human	Brain, Spine	<a href="#">L1</a>
Bustin	2020	<a href="#">103</a>	Rel	Indirect	RR	DM	Human	Cardiac	NA
Chen	2021	<a href="#">101</a>	Rel	Indirect	RR	DM	Human	Brain	NA
Liao	2020	<a href="#">36</a>	Diff	Indirect	RR	DM	Human	Brain	NA
Mazor	2018	<a href="#">92</a>	Rel	Indirect	RR	DM	Human	Brain	<a href="#">L1</a>
Milotta	2020	<a href="#">104</a>	Rel	Indirect	RR	DM	Human	Cardiac	NA
Milotta	2020	<a href="#">105</a>	Rel	Indirect	RR	DM	Human	Cardiac	NA
Qi	2019	<a href="#">88</a>	Rel	Indirect	RR	DM	Human	Cardiac	NA
Qi	2019	<a href="#">89</a>	Rel	Indirect	RR	DM	Human	Cardiac	NA
Roccia	2018	<a href="#">65</a>	Rel	Indirect	RR	DM	Human	Prostate	NA
Wang	2016	<a href="#">233</a>	Rel	Indirect	RR	DM	Simulation	Brain	NA
Dikaïos	2021	<a href="#">99</a>	Rel	Indirect	RR	DM	Human	Brain	NA
Song	2019	<a href="#">85</a>	Rel	Indirect	RR	LB	Human	Brain	NA
Bhave	2016	<a href="#">149</a>	Rel	Indirect	SCR	MF	Human	Brain	NA
Dong	2021	<a href="#">115</a>	Rel	Indirect	SCR	MF	Human	Brain	<a href="#">L1, L2</a>
Dong	2020	<a href="#">116</a>	Rel	Indirect	SCR	MF	Human	Brain	<a href="#">L1</a>
Feng	2021	<a href="#">117</a>	Rel	Indirect	SCR	MF	Human	Brain, Liver	NA
Feng	2011	<a href="#">336</a>	Rel	Indirect	SCR	MF	Human	Cardiac	NA
Gutjahr	2015	<a href="#">113</a>	Per	Indirect	SCR	MF	Rat	Cardiac	NA
Bilgic	2013	<a href="#">181</a>	DR	Indirect	SCR	MF	Human	Brain	<a href="#">L1</a>
Baltes	2005	<a href="#">337</a>	Flow	Indirect	SCR	MF	Human	Cardiac	NA
Cheng	2015	<a href="#">162</a>	Diff	Indirect	SCR	MF	Human	Brain	NA
Doneva	2010	<a href="#">47</a>	Rel	Indirect	SCR	MF	Human	Brain	NA
Hagio	2015	<a href="#">114</a>	Rel	Indirect	SCR	MF	Human	Cardiac	NA
Han	2019	<a href="#">151</a>	Rel	Indirect	SCR	MF	Human	Cardiac	NA
Huang	2012	<a href="#">111</a>	Rel	Indirect	SCR	MF	Human	Brain, Liver, Cardiac	NA
Huang	2012	<a href="#">110</a>	Rel	Indirect	SCR	MF	Human	Brain, Liver, Cartilage	NA



TABLE A3 (Continued)

Author	Year	References	Parameter	Category	Recon	Param	App	Organ	Data/code
Keerthivasan	2018	<a href="#">122</a>	Rel	Indirect	SCR	MF	Human	Brain, Knee, Carotid	NA
Lam	2020	<a href="#">123</a>	Rel	Indirect	SCR	MF	Human	Brain	NA
Lee	2016	<a href="#">182</a>	Rel	Indirect	SCR	MF	Human	Brain	<a href="#">L1</a>
Li	2012	<a href="#">189</a>	Rel	Indirect	SCR	MF	Mouse	Cardiac	NA
Zhitao	2019	<a href="#">129</a>	Rel	Indirect	SCR	MF	Human	Brain, Abdomen	NA
Ma	2018	<a href="#">163</a>	Diff	Indirect	SCR	MF	Human	Cardiac	NA
Ma	2020	<a href="#">159</a>	DR	Indirect	SCR	MF	Human	Brain	NA
Ma	2021	<a href="#">130</a>	Rel	Indirect	SCR	MF	Human	Brain	NA
Mandava	2018	<a href="#">140</a>	Rel	Indirect	SCR	MF	Human	Brain	NA
Mandava	2021	<a href="#">166</a>	Rel	Indirect	SCR	MF	Human	Brain, Knee	NA
Mani	2020	<a href="#">180</a>	Diff	Indirect	SCR	MF	Human	Brain	NA
Mani	2015	<a href="#">338</a>	Diff	Indirect	SCR	MF	Human	Brain	NA
McClymont	2016	<a href="#">63</a>	Diff	Indirect	SCR	MF	Rat	Cardiac	NA
Meng	2021	<a href="#">173</a>	Rel	Indirect	SCR	MF	Human	Brain	NA
Milshteyn	2018	<a href="#">174</a>	Rel	Indirect	SCR	MF	Rat	Body	<a href="#">L1</a>
Petzschner	2011	<a href="#">339</a>	Rel	Indirect	SCR	MF	Human	Brain	NA
Roeloffs	2020	<a href="#">135</a>	Rel	Indirect	SCR	MF	Human	Brain	<a href="#">L1</a>
Utzschneider	2020	<a href="#">190</a>	TSC	Indirect	SCR	MF	Human	Calf	NA
Utzschneider	2021	<a href="#">62</a>	TSC	Indirect	SCR	MF	Human	Calf	NA
Wang	2019	<a href="#">155</a>	Per	Indirect	SCR	MF	Human	Carotid	NA
Yaman	2020	<a href="#">156</a>	Rel	Indirect	SCR	MF	Human	Cardiac	NA
Zhang	2020	<a href="#">146</a>	Diff	Indirect	SCR	MF	Mouse	Abdomen	NA
Zhao	2015	<a href="#">164</a>	Rel	Indirect	SCR	MF	Human	Brain	NA
Zhou	2021	<a href="#">191</a>	Rel	Indirect	SCR	MF	Human	Cardiac, Brain	NA
Zhou	2015	<a href="#">340</a>	Rel	Indirect	SCR	MF	Human	Cartilage	<a href="#">L1</a>
Zhou	2015	<a href="#">148</a>	Rel	Indirect	SCR	MF	Human	Brain	NA
Zhu	2018	<a href="#">175</a>	Rel	Indirect	SCR	MF	Human	Brain	NA
Zhu	2020	<a href="#">176</a>	Rel	Indirect	SCR	MF	Human	Brain	NA
Cao	2021	<a href="#">145</a>	Rel	Indirect	SCR	MF	Human	Brain	NA
Cao	2022	<a href="#">152</a>	Rel	Indirect	SCR	MF	Human	Cardiac	NA
Dong	2022	<a href="#">136</a>	DR	Indirect	SCR	MF	Human	Brain	NA
kargas	2017	<a href="#">150</a>	Rel	Indirect	SCR	MF	Human	Cardiac	NA
Keerthivasan	2022	<a href="#">168</a>	Rel	Indirect	SCR	MF	Human	Liver	NA
Li	2021	<a href="#">124</a>	Rel	Indirect	SCR	MF	Human	Brain, Prostate	NA
Li	2022	<a href="#">125</a>	Rel	Indirect	SCR	MF	Human	Brain	NA
Liao	2021	<a href="#">185</a>	Diff	Indirect	SCR	MF	Human	Brain	NA

TABLE A3 (Continued)

Author	Year	References	Parameter	Category	Recon	Param	App	Organ	Data/code
Liu	2021	<a href="#">177</a>	Rel	Indirect	SCR	MF	Human	Cartilage	NA
Mao	2022	<a href="#">160</a>	Rel	Indirect	SCR	MF	Human	Cardiac	NA
Wang	2022	<a href="#">161</a>	Rel	Indirect	SCR	MF	Human	Liver	NA
Zhang	2022	<a href="#">186</a>	Rel	Indirect	SCR	MF	Human	Brain	<a href="#">L1</a>
Zhou	2022	<a href="#">147</a>	Rel	Indirect	SCR	MF	Human	Brain	NA
Mani	2017	<a href="#">179</a>	Diff	Indirect	SCR	MF	Human	Brain	NA
Wen	2020	<a href="#">172</a>	Diff	Indirect	SCR	MF	Human	Brain	NA
Asslander	2018	<a href="#">144</a>	Rel	Indirect	SCR	DM	Human	Brain	<a href="#">L1</a>
Hamilton	2020	<a href="#">119</a>	Rel	Indirect	SCR	DM	Human	Cardiac	NA
Hamilton	2019	<a href="#">120</a>	Rel	Indirect	SCR	DM	Human	Cardiac	NA
Zhao	2017	<a href="#">121</a>	Rel	Indirect	SCR	DM	Simulation	Brain	NA
Bermen	2015	<a href="#">143</a>	Rel	Indirect	SCR	DM	Human	Brain	NA
Golbabaee	2019	<a href="#">131</a>	Rel	Indirect	SCR	DM	Human	Brain	<a href="#">L1</a>
Jaubert	2020	<a href="#">137</a>	Rel	Indirect	SCR	DM	Human	Cardiac	NA
Jaubert	2019	<a href="#">138</a>	Rel	Indirect	SCR	DM	Human	Cardiac	NA
Cruz	2019	<a href="#">112</a>	Rel	Indirect	SCR	DM	Human	Brain	NA
Liu	2016	<a href="#">192</a>	Rel	Indirect	SCR	DM	Human	Gastric	NA
Tang	2018	<a href="#">97</a>	Rel	Indirect	SCR	DM	Phantom	Phantom	NA
Zhao	2018	<a href="#">118</a>	Rel	Indirect	SCR	DM	Human	Brain	NA
Zhao	2020	<a href="#">154</a>	Rel	Indirect	SCR	DM	Human	Brain	NA
Zhu	2015	<a href="#">194</a>	Rel	Indirect	SCR	DM	Human	Brain, Spine	NA
Zhu	2018	<a href="#">193</a>	Rel	Indirect	SCR	DM	Human	Cardiac	NA
Cao	2022	<a href="#">167</a>	Rel	Indirect	SCR	DM	Human	Brain	NA
Cao	2021	<a href="#">184</a>	Rel	Indirect	SCR	DM	Human	Brain	NA
Cruz	2022	<a href="#">141</a>	Rel	Indirect	SCR	DM	Human	Cardiac, Liver	NA
Han	2022	<a href="#">165</a>	Rel	Indirect	SCR	DM	Human	Heart	NA
Hu	2022	<a href="#">183</a>	Rel	Indirect	SCR	DM	Human	Brain	NA
Li	2021	<a href="#">187</a>	Rel	Indirect	SCR	DM	Human	Brain	NA
Cruz	2022	<a href="#">142</a>	Rel	Indirect	SCR	DM	Human	Cardiac	NA
Sen	2021	<a href="#">153</a>	Rel	Indirect	SCR	DM	Human	Brain	NA
Mickevicius	2022	<a href="#">128</a>	Rel	Indirect	SCR	DM	Human	Brain, Pelvic	<a href="#">L1</a>
Mickevicius	2021	<a href="#">127</a>	Rel	Indirect	SCR	DM	Human	Brain, Pelvic	NA
Pirkl	2022	<a href="#">134</a>	Rel	Indirect	SCR	DM	Human	Brain	NA
Velasco	2021	<a href="#">139</a>	Rel	Indirect	SCR	DM	Human	Cardiac	NA
Wang	2022	<a href="#">126</a>	Rel	Indirect	SCR	DM	Human	Brain	<a href="#">L1, L2</a>
West	2022	<a href="#">169</a>	Rel	Indirect	SCR	DM	Human	Brain	<a href="#">L1</a>
Golbabaee	2021	<a href="#">132</a>	Rel	Indirect	SCR	LB	Human	Brain	<a href="#">L1</a>
Li	2020	<a href="#">178</a>	Rel	Indirect	SCR	LB	Human	Brain	NA
Pirkl	2021	<a href="#">133</a>	Rel	Indirect	SCR	LB	Human	Brain	NA

TABLE A3 (Continued)

Author	Year	References	Parameter	Category	Recon	Param	App	Organ	Data/code
Zhang	2022	<a href="#">170</a>	Rel	Indirect	SCR	LB	Human	Brain	<a href="#">L1</a>
Chan	2019	<a href="#">204</a>	Rel	Indirect	VS	MF	Human	Prostate	NA
Darcot	2019	<a href="#">199</a>	Rel	Indirect	VS	MF	Human	Cardiac	NA
Hilbert	2019	<a href="#">41</a>	Rel	Indirect	VS	MF	Human	Brain	NA
Jiang	2005	<a href="#">195</a>	Diff	Indirect	VS	MF	Sheep	Cardiac	NA
Nagtegaal	2020	<a href="#">207</a>	Rel	Indirect	VS	MF	Human	Brain	NA
Svedin	2019	<a href="#">200</a>	Temp	Indirect	VS	MF	Phantom	Phantom	NA
Todd	2010	<a href="#">198</a>	Temp	Indirect	VS	MF	Ex vivo	Ex vivo	NA
Wen	2018	<a href="#">206</a>	Diff	Indirect	VS	MF	Human	Brain	NA
Fan	2022	<a href="#">201</a>	Per	Indirect	VS	MF	Human	Cardiac	NA
Lugand	2015	<a href="#">202</a>	Rel	Indirect	VS	MF	Human	Cardiac	NA
Piredda	2021	<a href="#">210</a>	Rel	Indirect	VS	MF	Human	Brain	NA
Buonincontri	2016	<a href="#">197</a>	Rel	Indirect	VS	DM	Rat	Brain	NA
Cao	2017	<a href="#">205</a>	Rel	Indirect	VS	DM	Human	Brain	NA
Cruz	2018	<a href="#">196</a>	Rel	Indirect	VS	DM	Human	Brain	<a href="#">L1</a>
Liao	2017	<a href="#">208</a>	Rel	Indirect	VS	DM	Human	Brain	NA
Marty	2017	<a href="#">66</a>	Rel	Indirect	VS	DM	Human	Cardiac	NA
Cao	2022	<a href="#">211</a>	Rel	Indirect	VS	DM	Human	Liver	NA
Pirk	2020	<a href="#">209</a>	DR	Indirect	VS	LB	Human	Brain	NA
Fu	2020	<a href="#">222</a>	Rel	Indirect	LB	MF	Human	Brain, Knee, Abdomen	NA
Gong	2022	<a href="#">215</a>	Per	Indirect	LB	MF	Human	Brain	NA
Yang	2019	<a href="#">225</a>	Rel	Indirect	LB	MF	Human	Cartilage	NA
Duan	2022	<a href="#">221</a>	Diff	Indirect	LB	MF	Human	Lung	NA
Gao	2021	<a href="#">219</a>	Rel	Indirect	LB	MF	Human	Brain	<a href="#">L1</a>
Aggarwal	2020	<a href="#">188</a>	Diff	Indirect	LB	MF	Human	Brain	<a href="#">L1, L2</a>
Hu	2021	<a href="#">212</a>	Diff	Indirect	LB	MF	Human	Brain, Breast	<a href="#">L1</a>
Mani	2020	<a href="#">213</a>	Diff	Indirect	LB	MF	Human	Brain	NA
Zibetti	2020	<a href="#">214</a>	Rel	Indirect	LB	MF	Human	Knee	NA
Ji	2021	<a href="#">220</a>	Rel	Indirect	LB	MF	Human	Brain	NA
Mani	2021	<a href="#">217</a>	Diff	Indirect	LB	MF	Human	Brain	NA
Mani	2022	<a href="#">216</a>	Diff	Indirect	LB	MF	Human	Brain	NA
Fatania	2022	<a href="#">218</a>	Rel	Indirect	LB	DM	Human	Brain	NA
Wu	2020	<a href="#">223</a>	Rel	Indirect	LB	LB	Human	Cartilage	NA
Shih	2021	<a href="#">224</a>	Rel	Indirect	LB	LB	Human	Liver	NA
Ben-Eliezer	2016	<a href="#">267</a>	Rel	Direct	MB	MB	Human	Brain, Spine	<a href="#">L1</a>
Dikaos	2020	<a href="#">286</a>	PR	Direct	MB	MB	Human	Liver	<a href="#">L1</a>
Gaur	2015	<a href="#">289</a>	Temp	Direct	MB	MB	Human	Brain	<a href="#">L1</a>
Guo	2017	<a href="#">298</a>	Per	Direct	MB	MB	Human	Brain	<a href="#">L1</a>

TABLE A3 (Continued)

Author	Year	References	Parameter	Category	Recon	Param	App	Organ	Data/code
Hu	2019	<a href="#">310</a>	Rel	Direct	MB	MB	Human	Cardiac, Brain	NA
Dong	2018	<a href="#">292</a>	Diff	Direct	MB	MB	Human	Brain	NA
Awate	2013	<a href="#">305</a>	Diff	Direct	MB	MB	Simulation	Brain	NA
Dong	2019	<a href="#">275</a>	Rel	Direct	MB	MB	Simulation	Brain	NA
Eliasi	2014	<a href="#">304</a>	Rel	Direct	MB	MB	Human	Cardiac	NA
Hilbert	2018	<a href="#">306</a>	Rel	Direct	MB	MB	Human	Brain, Knee, Prostate, Liver	NA
Hu	2015	<a href="#">279</a>	Rel	Direct	MB	MB	Phantom	Brain	NA
Knoll	2015	<a href="#">291</a>	Diff	Direct	MB	MB	Human	Brain, Knee	NA
Lankford	2014	<a href="#">282</a>	Rel	Direct	MB	MB	Human	Brain	NA
Maier	2019	<a href="#">299</a>	Rel	Direct	MB	MB	Human	Brain	<a href="#">L1</a>
Olafsson	2008	<a href="#">302</a>	Rel	Direct	MB	MB	Human	Brain	NA
Peng	2014	<a href="#">295</a>	Rel	Direct	MB	MB	Human	Brain	NA
Pesce	2019	<a href="#">268</a>	Diff	Direct	MB	MB	Human	Brain	NA
Raudner	2020	<a href="#">307</a>	Rel	Direct	MB	MB	Human	Spine	NA
Raudner	2021	<a href="#">308</a>	Rel	Direct	MB	MB	Human	Spine	NA
Roeloffs	2016	<a href="#">341</a>	Rel	Direct	MB	MB	Human	Brain, Liver	NA
Sbrizzi	2018	<a href="#">309</a>	Rel	Direct	MB	MB	Human	Brain	NA
Schneider	2020	<a href="#">280</a>	Rel	Direct	MB	MB	Human	Liver	NA
Sharma	2013	<a href="#">281</a>	Rel	Direct	MB	MB	Human	Liver	NA
Sumpf	2014	<a href="#">274</a>	Rel	Direct	MB	MB	Human	Brain	<a href="#">L1</a>
Sumpf	2011	<a href="#">265</a>	Rel	Direct	MB	MB	Human	Brain	NA
Sun	2019	<a href="#">301</a>	Diff	Direct	MB	MB	Human	Brain	NA
Sun	2015	<a href="#">300</a>	Diff	Direct	MB	MB	Human	Brain	NA
Tan	2017	<a href="#">311</a>	Flow	Direct	MB	MB	Human	Carotid	NA
Tran-Gia	2015	<a href="#">270</a>	Rel	Direct	MB	MB	Human	Brain	<a href="#">L1</a>
Van der Heide	2020	<a href="#">278</a>	Rel	Direct	MB	MB	Human	Brain	NA
Wang	2019	<a href="#">284</a>	Rel	Direct	MB	MB	Human	Cardiac	<a href="#">L1</a>
Wang	2017	<a href="#">283</a>	Rel	Direct	MB	MB	Human	Brain, Abdomen	NA
Wang	2020	<a href="#">285</a>	Rel	Direct	MB	MB	Human	Brain, Abdomen	<a href="#">L1, L2</a>
Wang	2018	<a href="#">296</a>	Rel	Direct	MB	MB	Human	Brain, Abdomen	NA
Welsh	2013	<a href="#">269</a>	Diff	Direct	MB	MB	Human	Brain	NA
Welsh	2011	<a href="#">266</a>	Diff	Direct	MB	MB	Human	Brain	NA
Wiens	2013	<a href="#">272</a>	Rel	Direct	MB	MB	Human	Leg, Knee, Liver, Cardiac	NA
Zhao	2015	<a href="#">276</a>	Rel	Direct	MB	MB	Human	Brain	NA
Zhao	2014	<a href="#">297</a>	Rel	Direct	MB	MB	Human	Brain	NA



TABLE A3 (Continued)

Author	Year	References	Parameter	Category	Recon	Param	App	Organ	Data/code
Zhao	2016	<a href="#">277</a>	Rel	Direct	MB	MB	Human	Brain	NA
Zhao	2016	<a href="#">273</a>	Rel	Direct	MB	MB	Human	Brain	NA
Zhu	2012	<a href="#">303</a>	Diff	Direct	MB	MB	Rat	Brain	NA
Hanhela	2022	<a href="#">294</a>	Rel	Direct	MB	MB	Mouse	Kidney	<a href="#">L1</a>
Hufken	2022	<a href="#">293</a>	Diff	Direct	MB	MB	Human	MSK	NA
Pesce	2021	<a href="#">290</a>	Diff	Direct	MB	MB	Human	Brain	NA
Shafieizargar	2021	<a href="#">287</a>	Diff	Direct	MB	MB	Mouse	Brain	NA
Zhu	2021	<a href="#">271</a>	Rel	Direct	MB	MB	Human	Brain	<a href="#">L1</a>
Jun	2021	<a href="#">314</a>	Rel	Direct	LB	LB	Human	Brain	NA
Liu	2019	<a href="#">312</a>	Rel	Direct	LB	LB	Human	Knee	NA
Liu	2020	<a href="#">313</a>	Rel	Direct	LB	LB	Human	Brain, Knee	NA
Liu	2022	<a href="#">315</a>	Rel	Direct	LB	LB	Human	Brain	NA
Liu	2021	<a href="#">316</a>	Rel	Direct	LB	LB	Human	Brain	NA

Abbreviations: Diff, diffusion; DM, dictionary matching; LB, learning-based; MB, model-based; MF, model fitting; Per, perfusion; PI, multicontrast PI; Rel, relaxometry; RR, regularized reconstruction; SCR, subspace constrained reconstruction; Spec, spectroscopy; Temp, temperature; TSC, tissue sodium concentration; VS, view-sharing.